

Nora M. Wilson

**Modulation Spectroscopies
for Characterization of
Photovoltaic Materials
and Devices**



Nora M. Wilson

Born 1990, in Rosala, Finland

Previous studies

Master of Science, Åbo Akademi University, 2015



Modulation Spectroscopies for Characterization of Photovoltaic Materials and Devices

Nora M. Wilson

Physics
Faculty of Science and Engineering
Åbo Akademi University
Åbo, Finland, 2024

Supervisor

Professor Ronald Österbacka
Åbo Akademi University
Åbo, Finland

Opponent and pre-examiner

Associate Professor Tracey M. Clarke
University College London
London, UK

Pre-examiner

Professor Nikolai Tkachenko
Tampere University
Tampere, Finland

ISBN 978-952-12-4365-3 (printed)
ISBN 978-952-12-4366-0 (digital)
Painosalama, Åbo, Finland 2024

PREFACE

This thesis is based on my research at Physics, Faculty of Science and Engineering, Åbo Akademi University under the supervision of Ronald Österbacka. I started my research for my master's thesis, after which I had the opportunity to pursue a Ph.D. degree in the same field. Throughout the several meandering years of research, Ronald has provided advice, understanding, and encouragement. For this I am very grateful. The project started with simulations and analytical calculations for Photoinduced Absorption, but evolved to include experimental work. I am grateful to Simon Sandén for teaching me how to operate the setup and explaining the usefulness of my results, and how they form more than just a fun exercise in mathematics. For the later portion of cwPA measurements I would like to thank Harri Aarnio for all the help and patience in revealing the experimental problems behind our seemingly non-physical results. For several discussions and clarifications on solar cell theory I thank Oskar Sandberg and Christian Ahläng. I would also like to thank our laboratory engineers, past and present, Kjell-Mikael Källman and Staffan Dahlström for helping a more theoretically minded physicist in getting to terms with experimental equipment.

During February 2020 I had the opportunity to visit Swansea University and participate in research for a month. I am grateful to Ardan Armin for the opportunity, and to Drew Riley and the rest of the group for the warm welcome and fascinating hours in the lab. For the valuable comments and feedback on this thesis, I thank the preliminary examiners Nikolai Tkachenko and Tracey Clarke.

Working at Åbo Akademi Physics has been wonderful, and I appreciate all my colleagues for the great atmosphere and company through the years. Having a work environment in which to feel at home is a true privilege. I would like to thank everyone in my family, who have always supported my endeavours and encouraged learning new things. Being married to another physicist gives ample opportunity to discuss mathematical derivations and tricky physical scenarios at home. However, more than that, I am grateful to Henrik for always providing love and support, and for lifting me up in times of doubt.

For financial support for the research I would like to acknowledge:

The Academy of Finland (project No. 279055)

Otto A. Malm Foundation

Alfred Kordelin Foundation

Fortum and Neste Foundation

The Society of Swedish Literature in Finland

The Swedish Cultural Foundation in Finland

Svenska tekniska vetenskapsakademien i Finland

CONTENTS

I	Introduction	I
1.1	Photovoltaic semiconductors	2
1.2	Working principle of a solar cell	4
1.3	Characteristics of the solar cell device	6
1.4	Recombination	8
1.5	Organic semiconductors	10
1.5.1	Generation of free charge carriers	11
1.6	Modulation spectroscopies	12
1.7	Aim and scope of this thesis	13
2	Continuous-wave photoinduced absorption	15
2.1	Working principle of photoinduced absorption	16
2.2	Interpreting cwPA	16
2.2.1	Square-wave generation	19
2.2.2	Sinusoidal generation	22
2.2.3	Trap-assisted recombination in cwPA	23
2.3	Measuring cwPA	23
2.3.1	High-frequency signal loss	25
2.3.2	Phase shifts	27
2.4	Results from cwPA	28
2.4.1	Identifying the recombination mechanism from low-frequency quadrature	29
2.4.2	Determining generation and lifetime from frequency dependence	30
3	Electromodulated-photoluminescence quantum efficiency	34
3.1	Theory of EM-PLQY	35
3.2	Measuring EM-PLQY	36
3.3	Experimental verification	38
	Summary	39
	Sammanfattning på svenska	40
	Bibliography	42

LIST OF INCLUDED PUBLICATIONS

This thesis is based on the following publications. The publications are included in the end of the thesis with permission from the publishers.

- I. *Method for characterizing bulk recombination using photoinduced absorption*
Nora M. Wilson, Simon Sandén, Oskar J. Sandberg, and Ronald Österbacka
Journal of Applied Physics **121**, 095701 (2017),
<https://doi.org/10.1063/1.4977505>
- II. *Characterization of the dominating bulk recombination in bulk-heterojunction blends using photoinduced absorption*
Simon Sandén, Nora M. Wilson, Oskar J. Sandberg, and Ronald Österbacka
Applied Physics Letters **108**, 193301 (2016),
<https://doi.org/10.1063/1.4949016>
- III. *Recognizing and correcting for errors in frequency-dependent modulation spectroscopy*
Nora M. Wilson, Harri Aarnio, and Ronald Österbacka
Physica Scripta **98**, 115042 (2023),
<https://doi.org/10.1088/1402-4896/ad03bf>
- IV. *Comparing the loss of charge carrier generation with the loss of V_{OC} at low temperatures in organic bulk-heterojunction blends*
Nora M. Wilson, Harri Aarnio, and Ronald Österbacka
Physica Scripta **98**, 115985 (2023),
<https://doi.org/10.1088/1402-4896/acff94>
- V. *Direct Quantification of Quasi-Fermi-Level Splitting in Organic Semiconductor Devices*
Drew B. Riley, Oskar J. Sandberg, Nora M. Wilson, Wei Li, Stefan Zeiske, Nasim Zarrabi, Paul Meredith, Ronald Österbacka, and Ardalan Armin
Physical Review Applied **15**, 064035 (2021),
<https://doi.org/10.1103/PhysRevApplied.15.064035>
CC BY 4.0 licence (creativecommons.org/licenses/by/4.0/)

AUTHOR'S CONTRIBUTION TO PUBLICATIONS

- I. The author planned the work together with the co-authors, wrote the code for and performed the numerical simulations, analyzed the simulation data, calculated the analytical approximations, and wrote the draft of the manuscript. The author finalized the paper together with the co-authors.
- II. This paper applied the methods presented in more detail in Paper I. The author performed all numerical simulations, and calculated analytical approximations relating reaction order and exponential trap-depth to low-frequency cwPA. The experimental work was executed by S. Sandén. The author finalized the paper together with the co-authors.
- III. The author planned the work together with the co-authors. The experimental work was carried out by the author, together with H. Aarnio. Based on the results, the author developed the correction procedure. The author wrote the draft of the manuscript and finalized the paper together with the co-authors.
- IV. The author planned the work together with the co-authors. The author measured V_{OC} for PTB7:PCBM and all cwPA data together with H. Aarnio. The author applied the correction procedure from Paper III and extracted lifetimes and generation rates from the cwPA data. The author wrote the draft of the manuscript and finalized the paper together with the co-authors.
- V. The author planned (with D. B. Riley and A. Armin) and built (with D. B. Riley) the first working version of the experimental EM-PLQY-setup. The author and D. B. Riley analyzed the first proof-of-concept measurements, not included in the paper. The data presented in the paper were measured by D. B. Riley and the rest of the research group at Swansea University. The author finalized the paper together with the co-authors.

ADDITIONAL PUBLICATIONS

Characterization of recombination in P3HT:fullerene blends: Clarifying the influence of interfacial states

Simon Sandén, Nora M. Wilson, Mathias Nyman, and Ronald Österbacka
Organic Electronics **42**, 131–140 (2017),

<https://doi.org/10.1016/j.orgel.2016.12.017>

Generation of Photoexcitations and Trap-Assisted Recombination in TQ1:PC₇₁BM Blends

Simon Sandén, Nora M. Wilson, Ergang Wang, and Ronald Österbacka
Journal of Physical Chemistry C **121**, 8211–8219 (2017),

<https://doi.org/10.1021/acs.jpcc.7b01607>

LICENCES OF FIGURES

I have published all illustrations produced for this work (excluding those re-produced from previous publications) under a CC BY 4.0 licence (creativecommons.org/licenses/by/4.0/). The individual DOI:s are found below and all figures as a collection via <https://doi.org/10.6084/m9.figshare.c.6982614.v1>

Figure 1.1	https://doi.org/10.6084/m9.figshare.24833184	1
Figure 1.2	https://doi.org/10.6084/m9.figshare.24829755	3
Figure 1.3	https://doi.org/10.6084/m9.figshare.24833190	5
Figure 1.4	https://doi.org/10.6084/m9.figshare.24829746	7
Figure 1.5	https://doi.org/10.6084/m9.figshare.24821355	9
Figure 1.6	https://doi.org/10.6084/m9.figshare.24821349	12
Figure 2.1	https://doi.org/10.6084/m9.figshare.24833193	15
Figure 2.2	https://doi.org/10.6084/m9.figshare.24829749.v2	17
Figure 2.3	https://doi.org/10.6084/m9.figshare.24808599	19
Figure 2.4	https://doi.org/10.6084/m9.figshare.24821352	20
Figure 2.5	Modified from https://doi.org/10.6084/m9.figshare.19086518.v1 (Licensed as CC BY 4.0, N M Wilson (2022)) and published as https://doi.org/10.6084/m9.figshare.24833187	24
Figure 2.6	https://doi.org/10.6084/m9.figshare.24834102	26
Figure 2.7	Reproduced (with modifications) from Paper III with the permission of IOP Publishing	27
Figure 2.8	https://doi.org/10.6084/m9.figshare.24829752	28
Figure 2.9	Reproduced from Paper II with the permission of AIP Publishing	29
Figure 2.10	Reproduced from Paper II with the permission of AIP Publishing	30
Figure 2.11	Reproduced from Paper III with the permission of IOP Publishing	31
Figure 2.12	Reproduced from Paper IV with the permission of IOP Publishing	31

Figure 2.13	Reproduced from papers III and IV with the permission of IOP Publishing	32
Figure 2.14	Reproduced from Paper IV with the permission of IOP Publishing	33
Figure 3.1	https://doi.org/10.6084/m9.figshare.24834441	34
Figure 3.2	Reproduced from Paper V, CC BY 4.0	38
Unnumbered figure in “Sammanfattning på svenska”: Slightly modified version of Figure 2.5 in Swedish, published as https://doi.org/10.6084/m9.figshare.24834324		

INTRODUCTION

To build a solar cell, one needs a material capable of transforming the energy of sunlight to electrical potential and current. This property is found in some semiconductors, for example in the conventionally used silicon and in novel materials made from organic compounds and perovskites. In these photovoltaic materials, photons from sunlight can excite electrons to energy levels where they are free to move and be extracted. The vacancies left by electrons, called holes, also contribute to the created current.

For solar cells, four processes are crucial to optimize: generation, recombination, transport, and extraction. Generation is the process in which a photon produces free charge carriers, and can involve several steps, as is the case for organic semiconductors. These often consist of a blend of two materials, and the excited electron-hole pair needs to find the interface between the two materials in order to separate and be extracted in different directions, as illustrated in Figure 1.1. Recombination is the inverse process of generation, where free charge carriers are lost as they return to their ground state.

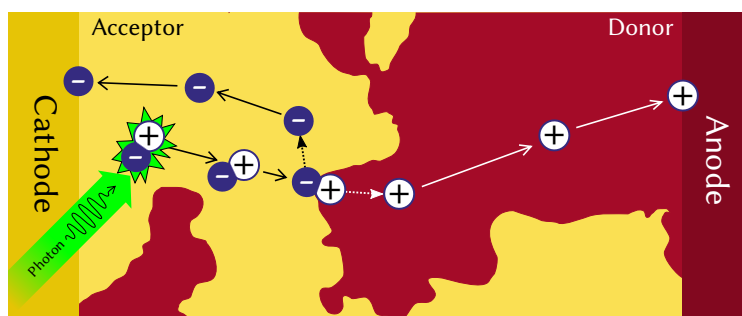


Figure 1.1: Schematic of an organic bulk-heterojunction solar cell, made from a blend of two materials. A photon creates an electron-hole pair which is separated at the interface of the materials, after which electrons and holes are transported and extracted separately.

In a solar cell under illumination, not connected to an external circuit, both generation and recombination occur. Charge carriers are generated and move randomly in the material until they inevitably recombine. All measurement techniques presented in this thesis are performed close to these, so-called open-circuit, conditions. In order to utilize charge carriers for electricity they must be transported to contacts, and from there extracted to an external circuit. The contacts can impact the behaviour of the solar cell significantly. As this work aims to present methods for studying the properties of the photovoltaic material in itself, I focus on open-circuit conditions and less on the impact of contacts.

To glean insight into the physics of photovoltaic materials I have used spectroscopic methods, specifically in forms that employ a periodically varying signal. These modulation spectroscopies achieve higher sensitivity to the measured quantity, such as absorption or luminescence, than an unmodulated measurement. All presented data come from organic semiconductor blends.

1.1 PHOTOVOLTAIC SEMICONDUCTORS

A set of isolated atoms offers states for several electrons with identical energy relative to vacuum. If the atoms are brought in close contact, the identical energy levels will split to avoid violating the Pauli exclusion principle. These states, close to each other in energy, form a continuous band. The manner in which electrons will occupy a given energy interval is described by the Fermi-Dirac distribution

$$\mathcal{F}(E) = \frac{1}{\exp[(E - E_F)/kT] + 1}, \quad (1.1)$$

where E_F is the Fermi level, k is the Boltzmann constant, and T is the temperature in Kelvin. The form of the distribution is illustrated in Figure 1.2. At $E = E_F$ half of the states are occupied, and going to lower (higher) energies the probability of a given state being occupied rapidly approaches 1 (0). For a semiconductor, E_F falls in a gap between bands, while for a conductor it falls in a continuous band [1]. For a conductor E_F determines the work function Φ , defined as the difference in energy between the vacuum level and E_F . The vacuum level is here defined as the energy of an electron just outside the surface, still affected by any electric potential of the solid.

In a semiconductor an energy gap E_G separates the excited states from the ground states. The states below and above the gap form the valence and conduction bands (delimiting the gap with the edges E_V and E_C). If the band gap is narrow enough, an electron in the valence band can be promoted to the conduction band by absorbing sunlight. Any excess energy will be lost via interaction with the lattice. In the nearly empty conduction band, electrons are free to move and form an electric current. In the valence band, the vacancy left by the electron can be treated as a particle with charge $+e$, a hole. With optimized device design a large portion of free charge carriers can be extracted and used for electrical energy, instead of decaying back to the ground state.

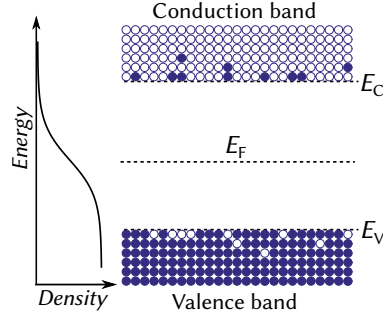


Figure 1.2: Illustration of the electron (filled blue circles) distribution in a semiconductor.

The densities of electrons and holes can, at thermal equilibrium in the dark, be described as [2]

$$n_e = N_C \exp \left(-\frac{E_C - E_F}{kT} \right) \quad (1.2)$$

$$n_h = N_V \exp \left(-\frac{E_F - E_V}{kT} \right), \quad (1.3)$$

where N_C (N_V) is the effective density of states in the conduction (valence) band. The equation requires $kT \ll E_G$ and $n_{e(h)} \ll N_{C(V)}$. In an intrinsic semiconductor, where all free electrons originate from the valence band, $n_e = n_h = n_i$, where n_i is the intrinsic density generated by thermal energy. Therefore, at equilibrium in the dark,

$$n_e n_h = n_i^2 = N_C N_V \exp \left(-\frac{E_G}{kT} \right). \quad (1.4)$$

An operating solar cell will, in addition to n_i , have photogenerated charge carriers. The photogenerated carriers will rapidly thermalize and find thermal equilibrium within the carrier populations in the bands [3]. Hence, they will follow a Fermi-Dirac distribution, but with the Fermi levels shifted towards the bands, to so-called quasi Fermi levels. The two quasi Fermi levels,

E_{FC} for the electrons in the conduction band and E_{FV} for the holes in the valence band, describe the densities as

$$n_e = N_{\text{C}} \exp\left(-\frac{E_{\text{C}} - E_{\text{FC}}}{kT}\right), n_h = N_{\text{V}} \exp\left(-\frac{E_{\text{FV}} - E_{\text{V}}}{kT}\right) \quad (1.5)$$

$$n_e n_h = n_i^2 \exp\left(\frac{E_{\text{FC}} - E_{\text{FV}}}{kT}\right). \quad (1.6)$$

The value $E_{\text{FC}} - E_{\text{FV}}$ is called the quasi Fermi level splitting (QFLS). Chapter 3 discusses a method for determining QFLS.

1.2 WORKING PRINCIPLE OF A SOLAR CELL

Charge carriers created homogenously in a photovoltaic semiconductor film do not have any incentive to move in a specific direction to create current. Adding two carefully chosen materials as contacts on each side of the film transforms the device into a solar cell. In the simplest case, a single photovoltaic material is sandwiched between two contacts. One of the contacts, the cathode, is often made from a metal with a Fermi level $E_{\text{F}}^{\text{cat}}$ close to, but below, the conduction band edge E_{C} of the semiconductor. A cathode with a Fermi level below E_{C} readily accepts electrons, as that will give them a small drop in energy. On the other side of the semiconductor, the anode works on the same principle, but in reverse, with a E_{F}^{an} slightly above the semiconductor valence band drawing holes out of the photovoltaic material. To understand how holes move, it is useful to consider them always striving towards higher-energy states, in opposite direction to electrons. The potential difference between the cathode and the anode drives electrons and holes into the external circuit, where they can be used to perform work.

The Fermi level depends both on the density of electrons and any electric potential present. As gradients both in potential and density will drive transport (drift and diffusion, respectively), E_{F} is related to charge carrier movement. It can be shown that a gradient in the Fermi level will always lead to a current, so materials in equilibrium will have constant Fermi levels across their interfaces [3]. The Fermi levels align by moving electrons to shift the electrostatic potentials.

An illustration of a photovoltaic semiconductor in the dark, before and after attaching the contacts, is shown in Figure 1.3a–b. The contacts are not

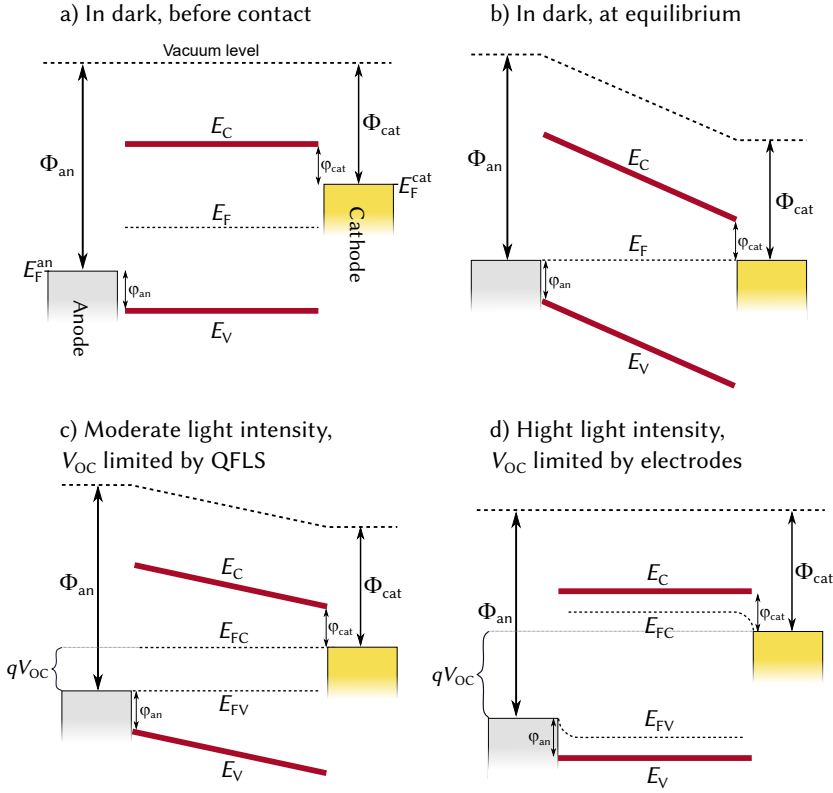


Figure 1.3: Energy levels for the materials in the dark (a) before and (b) after connecting the contacts to the semiconductor (no external circuit). (c) An illuminated solar cell where V_{OC} is limited by QFLS. (d) The cell under higher light intensity, where the electrodes limit the V_{OC} .

connected to an external circuit, i.e. the device is at open-circuit conditions. In this discussion I focus on the cathode and assume full symmetry with the processes illustrated at the anode. After contact, electrons will transfer from the cathode to the lower-energy anode, leading to a negative charge at the anode and a positive charge at the cathode. The charges create an electric field that raises the potential energy of the anode and lowers the energy of the cathode. When the contacts have reached the same energy the Fermi level will be constant throughout the device, but both the conduction and valence bands will have gradients due to the field. The band gap remains constant throughout the process, as does the difference in energy between E_F and E_C , called injection barrier φ_{cat} .

Illuminating the device generates additional charges, described by two quasi Fermi levels. It is energetically unfavourable for holes to be injected from the cathode, as they see a high barrier to the valence band, and it is unlikely that holes reach the cathode from the semiconductor, as it has a slope encouraging drift towards the anode. Therefore, the carriers crossing the cathode-semiconductor interface to establish equilibrium are mainly electrons. Thus, the cathode will align with E_{FC} and anode with E_{FV} , as illustrated in Figure 1.3c. As E_{FC} lies higher than E_F in the dark, equilibrium will be reached with a higher E_F^{cat} , meaning less steep slopes for E_V and E_C .

The voltage produced by the solar cell will equal the voltage between one contact at E_{FC} and one at E_{FV} . As the sample is at open-circuit conditions, we get an expression relating the ideal open-circuit voltage to the potential difference between the quasi Fermi levels, $V_{OC} = V_{QFLS}$.

Further increasing the light intensity widens the QFLS. Eventually the slope of E_C will flatten out, halting the inflow of additional electrons to the cathode and thereby the increase in E_F^{cat} . Any higher E_{FC} can not be utilized by the cathode. Instead, an increase of E_{FC} into the gap between E_F^{cat} and E_C will lead to E_{FC} remaining higher than E_F^{cat} throughout most of the device [4]. This situation is illustrated in Figure 1.3d. Close to the cathode electrons will be extracted despite the constant E_C , giving a quasi Fermi level that dips down towards E_F^{cat} [5]. The potential difference between anode and cathode will be defined by the injection barriers as $V_{OC} = E_G - \phi_{\text{cat}} - \phi_{\text{an}} = \Phi_{\text{an}} - \Phi_{\text{cat}}$.

In order to avoid the situation where V_{OC} becomes limited by the contacts' work functions, interlayer materials are often used. These are chosen so that E_F^{cat} becomes closer to E_C . This can be achieved e.g. by adding an electric dipole at the interface [6].

1.3 CHARACTERISTICS OF THE SOLAR CELL DEVICE

To characterize solar cells a JV-curve is often measured. This curve shows what the current density output J of the solar cell is at different voltages. An example is shown in Figure 1.4. The current density obtained at $V = 0$, when the solar cell electrodes are essentially connected to each other without any resistance, is called the short-circuit current density, J_{SC} . The only

current available here is the photocurrent, produced by the photogenerated carriers. When increasing the positive voltage, the current will eventually change sign as the externally applied voltage will inject large currents through the device. Applying a negative voltage will, with ideal contacts, not create any current.

The point at which no current flows through the cell, $J = 0$, is called open-circuit voltage V_{OC} , and corresponds to the potential difference present in the device when it is not connected to an external circuit. This thesis focuses on making measurements at V_{OC} conditions, as the equilibrium makes it easier to detangle different physical processes in the device. When the solar cell is in use we want a power output as large as possible. As power is given by $P = VI$ this point is found where one can draw a rectangle with as large as possible area between the JV-curve and the axes.

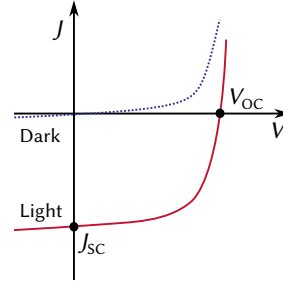


Figure 1.4: The current density versus voltage for a solar cell under light and in dark. Follows Equation 1.7.

The solar cell is constructed as a diode, as it blocks current in one direction and not in the other. To describe the behaviour of the solar cell, one can therefore use the Shockley ideal diode equation with the addition of a term J_L , accounting for the photocurrent [7].

$$J(V) = J_0(\exp(V/kT) - 1) - J_L, \quad (1.7)$$

where J_0 is called the dark saturation current. At $J = 0$ we can solve for voltage and receive $V_{OC} = kT \ln(J_0 + J_L)$. This simple temperature dependence is not always what is observed, as discussed in Paper IV, where we measured a V_{OC} that first increased with decreasing temperature but started to drop at low temperatures. This was attributed to contact effects.

To construct an efficient solar cell, we want as many incoming photons to result in outgoing electrons as possible. This is described by the external quantum efficiency (EQE), defined as the number of electrons extracted per photons incident on the cell. An EQE of 1 can never be reached as a material capable of producing electron-hole pairs from photons must necessarily experience the reverse process, i.e. radiative recombination. This is due to the

principle of detailed balance, stating that, in thermodynamic equilibrium, a process must be in equilibrium with its inverse [8, 9]. Carriers can also be lost to non-radiative recombination, but there is no fundamental requirement for it to occur. Finding solutions which suppress these processes is therefore of great interest in the field [10–12].

1.4 RECOMBINATION

The process in which photoexcitations are lost as electrons return to the valence band is called recombination. The properties of the carriers involved impact how the recombination rate scales with carrier density. A first order process, where the recombination rate is directly proportional to the electron density, can occur when an electron and hole created by the same photon recombine. This process is generally called geminate or, as in this work, monomolecular recombination (Figure 1.5a). The rate at which monomolecular recombination decreases the carrier density can be written $dn/dt = -n/\tau$, where τ is a lifetime.

If an electron and a hole moving freely meet and recombine, the process is called non-geminate or (direct) bimolecular recombination (Figure 1.5b). As the process requires an electron and a hole to meet, its rate is proportional to both electron and hole densities. For photogenerated charge carriers, these densities are equal and decay as $dn/dt = -\beta_{\text{bim}}n^2$, with β_{bim} called the bimolecular recombination coefficient. In organic semiconductors β_{bim} is often described by Langevin theory, giving the value $\beta_{\text{bim}} = e(\mu_e + \mu_h)/\epsilon_r\epsilon_0$, where e is the elementary charge, μ_e (μ_h) the electron (hole) mobility, and ϵ_r (ϵ_0) the relative (vacuum) permittivity [13, 14]. If the recombination event involves three carriers, as in Auger recombination, the rate will depend on the density to the power three, n^3 [2]. Non-integer powers of the density can arise from restrictions of movement, such as $dn/dt \propto n^{2.5}$ for two-dimensional bimolecular recombination [15]. In general, we can describe recombination via a recombination coefficient b and an arbitrary reaction order δ .

$$\frac{dn}{dt} = -bn^\delta. \quad (1.8)$$

Most semiconductors have some states available in the band gap. These states are localized to certain positions and can arise from impurities or de-

viations in the morphology. Such states act as traps for charge carriers, fixing them in a location. Recombination occurring between one free and one trapped charge carrier is called indirect or trap-assisted recombination (Figure 1.5c). The rate for this recombination type is directly proportional to the product of the densities of trapped and free carriers (of opposite charge), $\propto nn_t$.

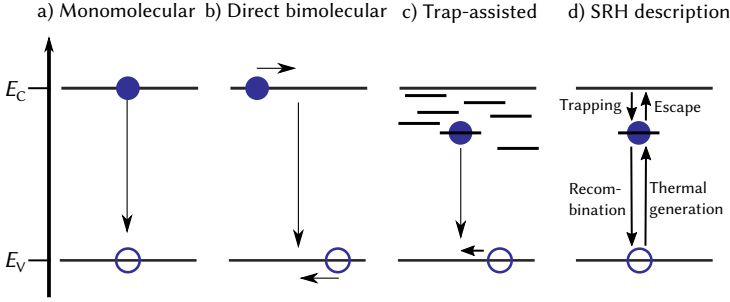


Figure 1.5: Illustration of (a–c) different recombination types and (d) the rates used in SRH statistics to calculate densities of trapped carriers.

To describe the density of trapped carriers we can as an approximation assume that they follow the quasi Fermi levels. As an example, consider traps distributed exponentially, so that their density below the conduction band decreases with decreasing energy as $N_t/E_{ch} \exp(-\frac{E-E_C}{E_{ch}})$ (with a symmetric distribution for holes above the valence band). Here, E_{ch} is the characteristic energy giving the mean trap depth and N_t the total trap density. For this case, Westerling et al. have derived the expression $n_t = N_t(n/N_C^*)$, relating the densities of trapped and free carriers [16]. Here, $N_C^* = N_C(\frac{kT}{w})(1 - \exp(-w/kT))$, with the states forming the conduction band distributed evenly in an interval of width w . The derivation of the expression requires that $E_{ch} \gg kT$. Now, recombination will be proportional to $nn_t \propto n^{1+E_{ch}/kT}$ [17]. Temperature-dependent reaction orders, in general, are a sign of trap-assisted recombination.

If we don't want to assume that the trapped carriers have equilibrated to a Fermi-Dirac distribution, we can turn to Shockley-Read-Hall (SRH) statistics [18, 19]. Assume that recombination occurs via two steps, trapping followed by recombination between trapped carrier and free carrier. The rate for trapping depends on the density of empty traps and free carriers. In addition, we need to describe rates for carriers escaping from the traps

and for being thermally generated. All these rates are illustrated in Figure 1.5d. Both escape and thermal generation rates depend on the energy needed to move upwards in the energy landscape, included in terms of the form $e^{-\text{energy difference}/kT}$. The rates are shown in more detail in Paper I and other works [2, 20]. Including all the rates that affect the density of trapped carriers gives a system of equations (one equation per trap depth) that can be numerically solved. This is the basis for the simulations of trap-assisted recombination in Paper I. For the application in the paper, the simulations will give the same result as the approximation discussed above as long as the trap depth is significantly deeper than kT .

In addition to bulk processes, accessible with the methods presented in this work, there may be surface recombination, occurring at the interfaces between photovoltaic materials and other components.

1.5 ORGANIC SEMICONDUCTORS

The interest in photovoltaic semiconductors made from organic compounds is built on the potential for flexible and cheap solar cells. Recent years have seen great leaps in efficiency owing to the development of new non-fullerene acceptors [21, 22]. Organic semiconductors generally have a disordered energy structure and disordered morphology. Usually, a light-harvesting material consisting of a mix of two types of molecules is used, forming a so-called bulk-heterojunction solar cell. The charge carriers are typically long-lived polarons, i.e. electrons and holes accompanied by the geometric distortion they cause around them.

Organic semiconductors characteristically consist of molecules with a backbone of carbon atoms connected by both σ - and π -bonds. The σ -bonds are localized at specific atoms while the π -bonds on several adjacent atoms form a continuous space in which electrons become delocalized. A typical example of such molecules are conjugated polymers, which form long chains along which the electrons can move. The highest-energy π -orbital occupied in the ground state is called the highest occupied molecular orbital (HOMO) and corresponds to the valence band edge. The lowest unoccupied molecular orbital (LUMO) corresponds to the conduction band edge. For bulk-heterojunction blends an effective medium model is sometimes a good approximation. This uses the HOMO level of the donor in combination with the

LUMO of the acceptor [23].

A significant difference between organic semiconductors and their typical inorganic counterparts is the lack of an ordered crystal structure [7]. The organic molecules can have randomness in their distribution, orientation and number of repeat units. Thus, each molecule experiences a slightly different surrounding, causing small shifts in the energy levels. Therefore, the bands do not have sharp edges, instead tails of localized states reach into the band gap. In addition to the randomness due to spatial variance, there may be additional localized states arising from defects, such as chemical deviations from the expected molecular structure. Localized states are called traps if they are so deep and distributed so sparsely that carriers have a low probability of leaving them. Often a Gaussian distribution is used to describe states in the bands and an exponential distribution for the states deeper in the gap [24–26].

The transport of carriers via localized states can be modelled by so-called hopping transport. Hopping is based on quantum mechanical tunnelling between the states [27, 28]. Although this fundamentally differs from the transport processes in inorganic crystalline semiconductors, using the framework of conduction and valence bands is often useful, for example when modelling recombination. As this thesis focuses on V_{OC} conditions, transport is not discussed further.

1.5.1 *Generation of free charge carriers*

When an electron is moved from the HOMO to the LUMO it will not yet be free, as it is bound by Coulomb interaction to the hole it left behind. This bound state, called exciton, is a singlet and has a short lifetime. The singlet ($\uparrow\downarrow$) will either recombine back to the ground state, flip an electron spin to become a triplet ($\uparrow\uparrow$), or separate, so that the charges become free from each other. Triplets are long-lived and can be observed with photoinduced absorption [29, 30]. In organic materials free electrons and holes form polarons. A polaron is a quasi particle, consisting of an electron or a hole combined with the geometric reorganization of the molecule that the charge causes [31]. Organic molecules are relatively soft and deform easily, making this a useful description of organic materials. The existence of strongly bound excitons is also of importance, specifically in organic semiconductors, due to their

low relative permittivity (ϵ_r commonly between 3 and 4), leading to weak screening. Inorganic semiconductors typically show much higher values, e.g. $\epsilon_r = 12$ for silicon.

In papers II and IV we study polarons with photoinduced absorption. The structural distortion creates two states in the band gap, one just below the LUMO and one just above the HOMO [32]. Polaron absorption can be identified by the P_1 and P_2 transitions, illustrated in Figure 1.6 [33, 34]. The relation $2P_1 + P_2 = E_g$ can aid in the identification of these in a spectrum. In addition, a polaron can in ordered molecular regions become delocalized, splitting both these energy levels into two [33].

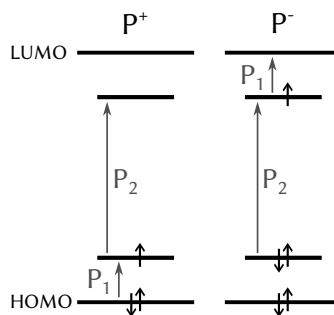


Figure 1.6: Polaron energy levels and their optical transitions, for positive and negative polarons.

The need to separate bound excitons is the reason for organic solar cells usually being constructed from a bulk-heterojunctions blend. One of the materials has energy levels suitable for accepting electrons and the other for donating electrons. After the exciton has reached the acceptor-donor interface and separated, the charges can be transported separately in each material phase. This is illustrated in Figure 1.1. To maximize the probability that an exciton will reach the acceptor-donor interface the materials need to be finely mixed but with phases continuous enough to allow for transport. Two charges, located on different sides of the interface, may be bound in a so-called charge transfer (CT) state. The role of the CT-state as an intermediary step in generation and recombination has been subject to extensive study [35].

1.6 MODULATION SPECTROSCOPIES

The development of modulation spectroscopy in the 1960's was made possible by the lock-in amplifier [36, 37]. When given a noisy signal, a lock-in amplifier's job is to filter out the only components which repeat at a frequency set by the user. Capable of singling out a signal thousands or millions of times smaller than the noise at other frequencies, the lock-in amplifier has become a valuable experimental tool [38]. The device is based on the orthogonality of

sinusoidal functions [39]. This states that averaging the product of two sine waves with different frequency will give 0 (regardless of the phase). The lock-in amplifier multiplies the incoming signal, which can be seen as a Fourier series with a plethora of different frequencies, with a sine wave created from the frequency specified by the user. The only constant terms in the product will come from the signal component with that frequency. Filtering out all time-dependent components will result in only the desired frequency component remaining.

The periodic response of the sample can be prompted by various means, such as light intensity, light wavelength, voltage, temperature, or stress [40]. Regardless of the stimuli, in spectroscopic techniques the output will always be electromagnetic radiation, either transmitted, reflected, or emitted. Some setups instead modulate a property of the measurement procedure, such as the detected wavelength.

Many users of modulation spectroscopy are mostly interested in inducing a small perturbation that influences the spectrum in order to eliminate featureless background signals and obtain a sharper spectrum [36, 37]. The result is the derivative of the spectrum with respect to the modulated parameter. Often a constant modulation frequency and intensity is used. There is however, additional knowledge to be gained from how the perturbation interacts with the optical properties. To learn this, one can vary some property of the modulation itself. This is discussed in more detail for photoinduced absorption in Chapter 2. The chapter also explores the information available from a dual-phase lock-in amplifier, giving both the component in-phase with the modulation and the component 90° out of phase.

The other type of modulation spectroscopy discussed in this thesis, electro-modulated-photoluminescence quantum efficiency, relies on an understanding of how the modulated current density modifies the measured photoluminescence. Here we do not strive for a spectrum, rather focusing on the change in total flux of photons.

1.7 AIM AND SCOPE OF THIS THESIS

The aim of this thesis is to present new ways of characterizing photovoltaic semiconductors and devices using modulation spectroscopies. Four of the five papers, which the thesis is based on, concern continuous-wave photoin-

duced absorption (cwPA). This is an optical pump-probe technique, using a modulated laser for creating photoexcitations in the material. Although the technique is routinely used to identify long-lived photoexcitation species in semiconductors, new insights can be gained from its frequency and intensity dependence. As cwPA does not require a complete solar cell, only a film of the photovoltaic material, it offers contact-free access to bulk processes. This thesis provides new routes to information about recombination, through determining the reaction order, and a toolbox for obtaining reliable cwPA-data despite imperfect equipment.

The fifth paper presents a new method, electromodulated-photoluminescence quantum efficiency, where a solar cell is subjected to a small periodic voltage while the photoluminescence is measured. Choosing the right voltage offset and amplitude gives access to the photoluminescence at open-circuit conditions, from which we can determine the quasi Fermi level splitting in the photovoltaic material.

In this work I provide useful tools for interpreting and performing experiments. Knowledge of how to overcome the limitations of experimental equipment is crucial for the advancement of material physics on a broad front, by scientists of different backgrounds and access to equipment. I also hope that, for some readers, this thesis may serve as an entry point into modulation spectroscopies.

CONTINUOUS-WAVE PHOTOINDUCED ABSORPTION

PHOTOINDUCED absorption is an optical technique based on generating photoexcitations with one light source and monitoring the absorption caused by them with another light source. As the change in transmission due to the photoexcitations is directly proportional to their density, we gain information about their generation and recombination dynamics. The advantage of the technique is that it is performed on a photovoltaic film, requiring no contacts. This enables studying the bulk of the material without the influence of contacts, which can limit extraction and induce recombination.

In continuous-wave photoinduced absorption (cwPA) the excitations are continuously generated with a periodically varying intensity. This chapter presents methods for analysing frequency and intensity dependence and shows how to correct for experimental limitations. The measurements presented here were performed on organic semiconductors, in which long-lived charged excitations, such as polarons, often are of interest. Therefore, the discussion is focused on charge carriers, but cwPA can also be used to observe neutral excitations.

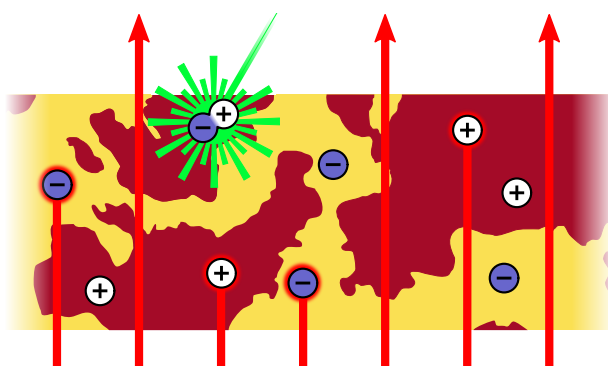


Figure 2.1: Schematic of the principle of photoinduced absorption in an organic semiconductor. A pump light (green laser) generates excitons that produce polarons, which absorb some of the probe light (red).

2.1 WORKING PRINCIPLE OF PHOTOINDUCED ABSORPTION

Photoinduced absorption is a pump-probe technique, that uses two light sources [41]. The pump light creates photoexcitations, and thus needs to have a photon energy high enough to excite the material. Often a laser is used. For the probe light a broad spectrum of longer wavelengths, that do not excite the sample, is desired. From this spectrum, the user can, e.g. with a monochromator, choose a wavelength at which a certain charge carrier or other excitation absorbs in order to study the dynamics of that species.

When studying photoexcitations, all interest lies in absorption induced by the pump light and not absorption present in the unexcited sample. Therefore, the absorption is always studied in relation to this baseline. Normalizing by the unexcited transmission also eliminates the influence of light loss due to geometry and optics, and variation in detector sensitivity at different wavelengths. By blocking the probe light, the luminescence can be measured. It is then subtracted from the raw optical signal, ensuring that only transmitted light is analysed.

We define PA as the decrease in transmission due to photogenerated carriers, normalized to the transmission without photogeneration: $-\Delta\mathcal{T}/\mathcal{T}$. With linear absorption in a thin film, the absorption will only depend on the absorption cross-section σ , the carrier density n , and the film thickness d [42–44]. When $n\sigma d \ll 1$

$$PA = -\frac{\Delta\mathcal{T}}{\mathcal{T}} = n\sigma d. \quad (2.1)$$

Here, it has been assumed that the impact of changes in reflection is negligible compared to absorption. For a thick film, d could be replaced by the approximate effective optical thickness $d_{\text{eff}} \approx 1/\alpha_L$, where α_L is the absorption coefficient [44]. Also note that a thick film would have a carrier density that depends on depth.

2.2 INTERPRETING CWPA

To relate photoinduced absorption to recombination and generation, we recall the previously presented equation governing carrier density via an arbitrary reaction order, Equation 1.8

$$\frac{dn(t)}{dt} = G(t) - bn(t)^\delta.$$

Here, the density of thermally generated carriers is assumed to be negligible compared to that of photogenerated ones. Sometimes it is more practical to work with an effective monomolecular lifetime, encapsulating the recombination dynamics into a density-dependent lifetime τ_δ using $n/\tau_\delta = bn^\delta$. Evaluating this near steady-state density, where the generation is constant $G(t) = G = bn^\delta$, gives

$$\tau_\delta = \frac{G^{-1+1/\delta}}{b^{1/\delta}}. \quad (2.2)$$

Using a periodically varying pump light makes $G(t)$ and $n(t)$ periodic. Choosing different shapes for the modulation gives slightly different dynamics, here we will discuss sinusoidal and square-wave generation.

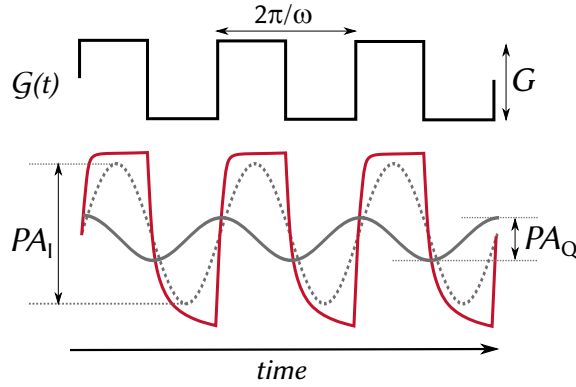


Figure 2.2: Illustration of the PA-signal (bottom red) resulting from a square-wave excitation (top). The two grey curves illustrate the lowest Fourier components, corresponding to the in-phase and quadrature.

Assume that the modulation is periodic with the main component $\cos(\omega\tau)$. The periodic density can be expanded in a Fourier series,

$$n(t) = \frac{a_0}{2} + \sum_{j=1}^{\infty} (a_j \cos j\omega t + b_j \sin j\omega t). \quad (2.3)$$

We use a lock-in amplifier to exclusively select the part of the signal that varies with the same frequency as the pump light. The lock-in amplifier will therefore only see the first components ($j = 1$) in the series. These are called

the in-phase and quadrature. Multiplying with σd , to get the photoinduced absorption, the components become

$$PA_I = \frac{\sigma d \omega}{\pi} \int_0^{2\pi/\omega} n(t) \cos(\omega t) dt \quad (2.4)$$

$$PA_Q = \frac{\sigma d \omega}{\pi} \int_0^{2\pi/\omega} n(t) \sin(\omega t) dt. \quad (2.5)$$

The in-phase PA_I has the same frequency and phase as the pump light, while the quadrature PA_Q has the same frequency but is phase shifted by 90° . This is illustrated in Figure 2.2 for square-wave generation. If the sample responds quickly to the pump light most of the signal will be in phase with the modulation and PA_I will be large. Conversely, a slow response leads to a larger quadrature.

Often we work with the signal in polar form, as radius and phase. The radius (amplitude) signal is defined as $PA_R = \sqrt{PA_I^2 + PA_Q^2}$ and the phase as $\theta = \arctan(PA_Q/PA_I)$. Conversely, we can calculate the in-phase and quadrature as $PA_I = PA_R \cos(\theta)$ and $PA_Q = PA_R \sin(\theta)$.

To gain insight into the dynamics of the charge carriers cwPA can be studied as a function of modulation frequency or intensity. In both cases, the behaviour is most easily analysed in two regimes: $\omega\tau \gg 1$ and $\omega\tau \ll 1$, where τ (or τ_δ) describes the effective lifetime of the carriers studied. Figure 2.3 illustrates typical curves and what information can be gained from which features (details in Table 2.1). Specifically, it illustrates how to determine reaction order δ , generation rate G , and lifetime τ . I discuss the calculations behind the expressions in sections 2.2.1–2.2.2. I analyse cwPA using an effective reaction order δ , stemming either from bimolecular recombination, possibly restricted by geometry, or from trap-assisted recombination.

The radius signal will approach whichever component, PA_I or PA_Q , that is larger in each regime. Thus, if the user only has access to PA_R , as might be the case if there are complex phase shifts caused by the setup, they can still access half of the slopes illustrated. If two different types of photoexcitations contribute to the signal, the shift between the regimes becomes more gradual and the different types may dominate different regimes.

When trying to reach the limits $\omega\tau \ll 1$ or $\omega\tau \gg 1$, to use the analytical approximations applicable there, it is helpful to consider the difference

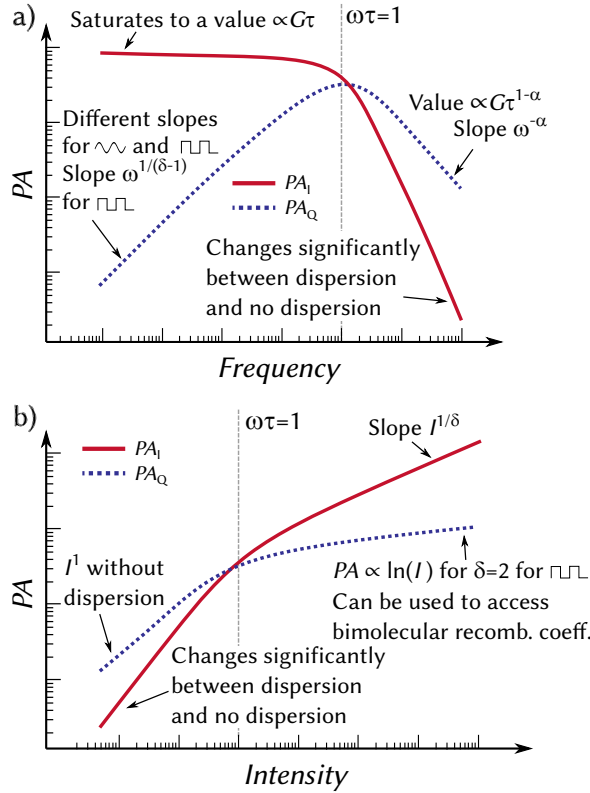


Figure 2.3: Some features in the behaviour of the in-phase and quadrature useful for gaining insight into charge carrier dynamics. Note the log-log scale. Full expressions in Table 2.1.

between intensity- and frequency-dependent measurements. When increasing ω one order of magnitude $\omega\tau$ will also increase by a factor of 10. To increase $\omega\tau$ by one order of magnitude via intensity, the change needs to be $0.1^{\delta/(\delta-1)}$ (using Equation 2.2). For $\delta = 2$ this evaluates to 0.01. The setup user must thus have the equipment to change the intensity several orders of magnitude more than the frequency to achieve the same breadth in observable behaviours.

2.2.1 Square-wave generation

Assume that the pump light intensity varies as a square wave with angular frequency ω . After a short stabilization period, the charge carrier density will reach a quasi steady state that varies with the same frequency. The generation

$G(t)$ will flip between G and 0. At the generation plateaus the carrier density will rise until it reaches steady state, i.e. when the recombination equals the generation. The lower the frequency, the more time the system has to respond and the closer to a square wave the response will be. For very high frequencies, the density will not reach the plateau and will be rising until the generation switches off, after which it starts to sink.

This case has been studied for bimolecular and monomolecular recombination by others [45–48]. For any natural number δ , Equation 1.8 does have an exact solution for the plateau of a square wave, but it is very complex and does not offer understanding of the behaviour [49]. Instead, we will attempt approximate solutions for the regimes $\omega\tau \ll 1$ and $\omega\tau \gg 1$.

When $\omega\tau \ll 1$, the density will quickly rise to the steady-state value $n_{ss} = (G/b)^{1/\delta}$ when the generation is switched on. When the generation is switched off the density will drop, but this decay is not as fast as the rise to steady state.* The behaviour is illustrated in Figure 2.4a.

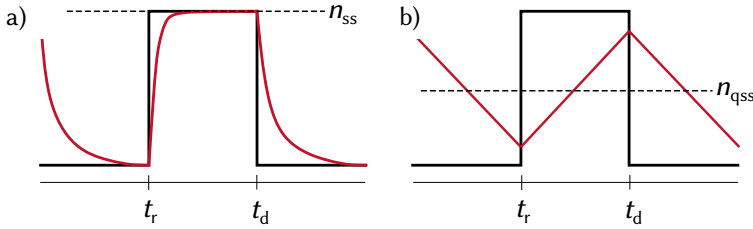


Figure 2.4: Illustration of the density response (red) to square-wave modulation (black) for (a) low frequency and (b) high frequency.

To obtain an approximate solution for low frequencies assume that the rise is instantaneous. Solving Equation 1.8 for the decay, gives the derivation detailed for PA_Q in the appendix of Paper I. The result (for $\delta > 2$) is

$$PA_Q \approx \frac{\sigma d}{\pi} \left(\frac{\omega}{b(\delta-1)} \right)^{1/(\delta-1)} \int_0^\pi \cos(v) v^{1/(1-\delta)} dv \propto \omega^{1/(\delta-1)}. \quad (2.6)$$

* This can be seen by considering the slopes (see Figure 2.4a for definitions). Instantly after $t = t_r$ the slope of $n(t)$ is $[dn/dt]_{n=0} = G$ and instantly after t_d the slope is the same but with a opposite direction: $[dn/dt]_{n=n_{ss}} = -G = -bn_{ss}^\delta$. Thus, the decay starts just as steep as the rise. Consider the second derivatives. For t_r the slope change is $[d^2n/dt^2]_{n=0} = 0$ and for t_d it is $[d^2n/dt^2]_{n=n_{ss}} = [-\delta bn^{\delta-1}dn/dt]_{n=n_{ss}} = \delta bn_{ss}^{\delta-1}G$. The positive change in slope for t_d means that the decay will start to slow down while the rise continues with the same slope until a significant amount of carriers have formed.

Using the same substitutions and approximations to derive PA_I gives analogously (when the decay starts at $t = \pi/2$)[†]

$$PA_I \approx \frac{G\tau\sigma d}{\pi} \int_{-\pi/2}^{\pi/2} \cos(v) dv = \frac{2G\tau\sigma d}{\pi} \propto G^{1/\delta}. \quad (2.7)$$

The case of $\delta = 2$ has been studied by Westerling et al. [47]. For $\omega\tau \ll 1$ this gives a logarithmic behaviour for PA_Q

$$PA_Q \approx \frac{\omega\sigma d}{2\pi\beta_{\text{bim}}} \ln \left(\frac{CG\beta_{\text{bim}}}{\omega^2} \right), \quad (2.8)$$

where $C \approx 1.461$ and β_{bim} is the bimolecular recombination coefficient. Westerling et al. presented this equation for a thick film, where the additional term of $e^{-\alpha_1 d/2}$ appears inside the logarithm. Using this relation we can determine β_{bim} from the slope of an intensity-dependent measurements on a lin-log plot if σ and d are known. In Paper I we show how Equation 2.6 becomes a poorer description of the low-frequency quadrature as $\delta = 2$ approaches 2, as expected when approaching the logarithmic behaviour.

When $\omega\tau \gg 1$ the slope of $n(t)$ will not have time to change much before the generation switches value. Thus, we will eventually reach a quasi steady state when the density varies close to a triangle wave with the same slope of G going up and down, illustrated in Figure 2.4b. The density will oscillate around a quasi-steady state density n_{qss} , at which the rise and decay slopes are equal but of opposite sign $G - bn_{\text{qss}}^\delta = bn_{\text{qss}}^\delta \implies n_{\text{qss}} = (G/2b)^{1/\delta}$. A solution for this situation has been calculated for mono- and bimolecular recombination by Westerling et al. [47]. The dependence on ω and G is the same as for the sinusoidal generation, discussed below. In Paper I simulations confirm that this is also the case for higher reaction orders.

†

$$\begin{aligned} PA_I &= \frac{\omega\sigma d}{\pi} \int_{-\pi/2\omega}^{3\pi/2\omega} \cos(\omega t) n(t) dt \\ &= \frac{\omega\sigma d}{\pi} \int_{-\pi/2\omega}^{\pi/2\omega} \cos(\omega t) n_{\text{ss}} dt + \frac{\sigma d}{\pi} \left(\frac{\omega}{b(\delta-1)} \right)^{1/(\delta-1)} \int_{\pi/2}^{3\pi/2} \cos(v) v^{1/(1-\delta)} dv \\ &= \frac{G\tau\sigma d}{\pi} \int_{-\pi/2}^{\pi/2} \cos(v) dv + \frac{\sigma d}{\pi} \left(\frac{\omega}{b(\delta-1)} \right)^{1/(\delta-1)} \int_{\pi/2}^{3\pi/2} \cos(v) v^{1/(1-\delta)} dv. \end{aligned}$$

Where we use $\tau_\delta = b^{-1/\delta} G^{1/\delta-1}$ (Equation 2.2) to get $n_{\text{ss}} = (G/b)^{1/\delta} = (G/(\tau^{-\delta} G^{1-\delta}))^{1/\delta} = G\tau$. Both integrals converge when $\delta > 2$. The first term does not have a ω dependence and will dominate over the second when $\omega \rightarrow 0$ or $\tau \rightarrow \infty$.

2.2.2 Sinusoidal generation

In addition to square waves, a sinusoidal modulation is often used, described by $G(t) = \frac{1}{2}G(1 + \cos(\omega t))$. An approximate solution, satisfying the first harmonic, has been derived for the bimolecular case by Westerling et al [50]. The solution can be generalized for an arbitrary reaction order δ by replacing the bimolecular lifetime with τ_δ from Equation 2.2.

$$PA_I = \frac{G\tau_\delta}{2} \left(\frac{\sqrt{F(\omega, \tau_\delta)}}{(\omega\tau_\delta)^2 + F(\omega, \tau_\delta)} \right) \quad (2.9)$$

$$PA_Q = \frac{G\tau_\delta}{2} \left(\frac{\omega\tau_\delta}{(\omega\tau_\delta)^2 + F(\omega, \tau_\delta)} \right), \text{ where} \quad (2.10)$$

$$F(\omega, \tau_\delta) = 1 - \frac{(\omega\tau_\delta)^2}{2} + \frac{1}{2}\sqrt{((\omega\tau_\delta)^2 + 2)^2 - 2}.$$

Table 2.1 shows how these expressions depend on intensity and frequency at the limits of $\omega\tau_\delta$. The high-intensity dependence of $PA_I \propto I^{1/\delta}$ has long been used to distinguish between monomolecular and bimolecular recombination [41]. Note that all expressions show a power law dependence on intensity (which is directly proportional to generation) or frequency. At low frequencies PA_I will saturate to a value directly proportional to $G\tau_\delta$, whereas the high-frequency PA_Q will be directly proportional to G but be independent of τ . Both of these are useful when interpreting temperature-dependent behaviour in Section 2.4.

Several experiments show a signal that falls off slower at high frequencies than equations 2.9–2.10 would predict. To explain this a Cole-Cole type equation was suggested by Epshtein et al. [51–53]. This type of function is connected to dispersive relaxation processes and often provides a good fit for cwPA results [54–58]. The resulting equations are [59]

$$PA_I = \frac{\frac{1}{2}G\tau\sigma d[1 + \cos(\frac{\alpha\pi}{2})(\omega\tau)^\alpha]}{1 + 2(\omega\tau)^\alpha \cos(\frac{\alpha\pi}{2}) + (\omega\tau)^{2\alpha}} \quad (2.11)$$

$$PA_Q = \frac{\frac{1}{2}G\tau\sigma d \sin(\frac{\alpha\pi}{2})(\omega\tau)^\alpha}{1 + 2(\omega\tau)^\alpha \cos(\frac{\alpha\pi}{2}) + (\omega\tau)^{2\alpha}}, \quad (2.12)$$

where $0 < \alpha < 1$ is the dispersion coefficient. A microscopical understanding is still lacking for this semi-empirical proposition. The main differences caused by these equations arise in the high-frequency regime, for example

the slope of $PA_Q \propto \omega^{-1}$ changes to $\omega^{-\alpha}$. Results for these equations at the limits, after inserting τ_δ , are shown in Table 2.1.

Table 2.1: Summary of the dependence on intensity ($I \propto G$) and modulation frequency (ω) at the limits of $\omega\tau_\delta$, for $\delta > 2$. For $\delta = 2$ the expression for square-wave generation $PA_Q \omega\tau_\delta \ll 1$ changes to Equation 2.8, the rest of the row still holds.

	$\omega\tau_\delta \ll 1$		$\omega\tau_\delta \gg 1$	
	PA_I	PA_Q	PA_I	PA_Q
Square wave	$I^{1/\delta}$	$\omega^{1/(\delta-1)}$	$I^{2-1/\delta} / \omega^2$	I / ω
Sinusoidal	$I^{1/\delta}$	$I^{2/\delta-1} \omega$	$I^{2-1/\delta} / \omega^2$	I / ω
Sin. with dispersion	$I^{1/\delta}$	$I^{(\alpha+1)/\delta-\alpha} \omega^\alpha$	$I^{1+\frac{(1-\delta)(1-\alpha)}{\delta}} / \omega^\alpha$	$I^{1+\frac{(1-\delta)(1-\alpha)}{\delta}} / \omega^\alpha$

2.2.3 Trap-assisted recombination in cwPA

A system where trap-assisted recombination is the dominating recombination mechanism will show a temperature-dependent reaction order, as the movement of trapped carriers is thermally activated. An effective reaction order was presented for an exponential trap distribution in Section 1.4, $\delta = 1 + E_{\text{ch}}/kT$. Using this in Table 2.1 neatly gives the low-frequency quadrature for a square-wave generation as $\omega^{kT/E_{\text{ch}}}$. This description fails when kT approaches E_{ch} (when $\delta \rightarrow 2$) or when the temperature gets very high (number of thermally generated carriers large). How well the PA-signal follows this effective reaction order is explored by comparing to simulations in Paper I. If the distributions for electrons and holes are asymmetrical, E_{ch} for the shallower trap determines the reaction order [17].

For a Gaussian distribution, no analytical approximations for the reaction order were found in this work and simulations showed a reaction order that, in addition to T , depended on ω and G .

2.3 MEASURING CWPA

The cwPA-setup used for the datasets in Section 2.4 is illustrated in Figure 2.5. Following the flow of information through the setup we start at the lock-in amplifier (Stanford Research Systems SR 830 DSP) with the sinusoidal reference signal with a frequency chosen by the user. This reference is used by

the lock-in amplifier to analyse the measured optical signal and by a function generator (Stanford Research Systems DS345) to generate a wave of desired shape. The amplitude and shape should be suitable for the driver unit of an optical modulator, to which the signal is sent. We use a chopper (Stanford Research Systems) for square-wave generation at low and moderately high frequencies (up to ca 4 kHz). For higher frequencies (up to 100 kHz) we use an acousto-optic modulator (Neos Technology) which will modulate an optical signal to the same shape as the signal from the frequency generator. In this work, it was only used with a sinusoidal shape.

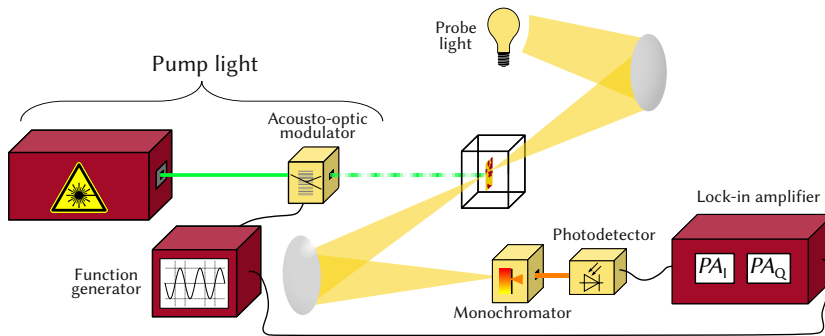


Figure 2.5: Schematic of the measurement setup used in continuous-wave photoinduced absorption (cwPA). A periodically modulated (by acousto-optic modulator or chopper) laser generates free charge carriers, which cause absorption of the probe light. The resulting change in transmission for a specific wavelength is then recorded as in-phase and quadrature by the lock-in amplifier.

The pump light starts as a continuous light beam, created by an argon ion laser (Coherent Innova) at a wavelength of 514 nm. The beam is then guided through the optical modulator, which shapes the periodic intensity. The optics guide the modulated beam to fall as evenly as possible on the sample. The sample is a film made from photovoltaic material, in which the pump light wavelength can create long-lived free charge carriers. The sample is placed in a cryostat to enable temperature control (liquid-nitrogen-cooled cryostat Janis Research, temperature controller LakeShore DRC-93CA).

The probe light, giving continuous light with a broad mix of wavelengths, comes from a tungsten lamp. The light is guided to the sample through a long-pass filter, ensuring that no high-frequency light from the probe light excites the sample. The sample is angled so that the probe light passes through

it perpendicular to the thin film. The transmitted probe beam is guided by a mirror to the monochromator (ARC SpectraPro-300i). As the monochromator grating will transmit both the desired wavelength and its multiples, a filter is placed in front of it to cut off these higher orders.

After passing the monochromator the beam arrives at the photodetector. Depending on the studied wavelength we use different detectors. These are silicon, germanium, or liquid-nitrogen-cooled InSb detectors. All frequency-dependent measurements were done at wavelengths suitable for silicon detectors. The detectors impose severe limitations at high frequencies, detailed below and in Paper III. From the detector, the signal goes via a pre-amplifier (Femto DHPCA 100) and finally the signal reaches the lock-in amplifier. The lock-in amplifier detects the signal, compares it to the reference, and outputs two results, corresponding to two orthogonal Fourier components, as discussed earlier. Ideally, these would be PA_I and PA_Q , but in most situations, some phase shifts need to be corrected for before obtaining these, as discussed below and in Paper III. In addition to these corrections, there might be some (frequency-dependent) background disturbances that need to be subtracted from the raw signal. To investigate this, all setups should be checked with a frequency-dependent measurement without any light sources reaching the detector. An example is discussed in Paper III.

2.3.1 *High-frequency signal loss*

To ensure reliable results the setup user must be aware of any limitations of their detector. A detector that does not respond fast enough for the chosen frequency will result in a loss of signal at high frequencies. To understand this, consider a square-wave light signal hitting a slow detector. When the square wave goes to zero the signal reported by the detector will start decaying. If the detector is too slow the signal will not reach zero before the square wave switches back to its plateau value. Similarly, the rise is cut off before the signal plateaus. This is seen in Figure 2.6a as the response to a square wave for different frequencies. As the lock-in amplifier only sees the amplitude of the periodic signal supplied by the detector, this shows up as a loss of PA-signal.

In order to correct for this loss the setup user needs to investigate the detector's response to a periodic light source with an amplitude that stays constant throughout all frequencies. As the lock-in amplifier only works with the first harmonics of any signal the shape of the signal is not crucial, mak-

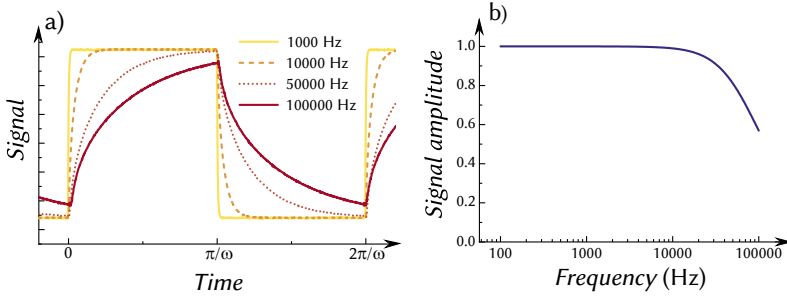


Figure 2.6: Illustration of the signal loss caused by a slow photodetector. (a) The response to a square wave for increasing frequencies, with loss of amplitude. (b) Example of relative loss of amplitude as function of frequency, following Equation 2.13 with $\tau_d = 2.3 \mu\text{s}$.

ing it possible to correct for the loss in a PA-signal of unknown shape. When a function describing the percentual loss is determined, any measured value can be divided with the value at that frequency. An example of such a function is shown in Figure 2.6b.

A possible pitfall is a signal loss that depends on wavelength. This might occur when longer wavelengths penetrate deeper into the semiconductor of the photodetector [60]. If carriers are generated beyond the depletion region, the transport of these carriers becomes very inefficient. Therefore, the response time of the detector becomes significantly longer for long wavelengths. An example is shown in Figure 2.7, where an increasing wavelength drastically increases the signal loss.

In Paper III we characterized two detectors, one of which showed a wavelength dependence and the other not. For the wavelength-independent detector we found an exponential decay, characterized by the decay time τ_d , to be a good description of the response. This behaviour deforms an incoming sine wave so that the output has a time-dependent component given by

$$\sin \omega t \mapsto \frac{\omega \tau_d \cos \omega t - \sin \omega t}{(\omega \tau_d)^2 + 1}. \quad (2.13)$$

The derivation is found in the supplemental material of Paper III. The amplitude of the signal will be $\propto 1/\sqrt{(\omega \tau_d)^2 + 1}$, which is the function illustrated by Figure 2.6b. In this example almost half of the signal is lost at 100 kHz, highlighting the importance of such corrections.

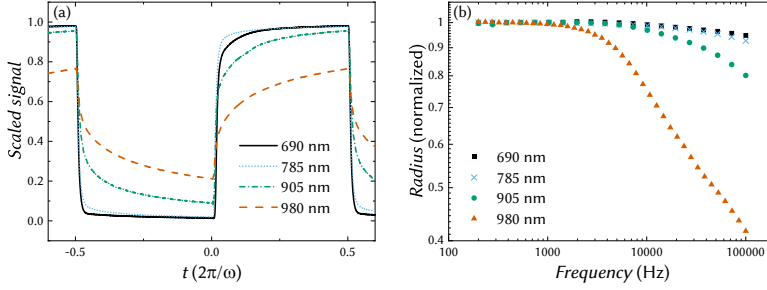


Figure 2.7: Illustration of the signal loss caused by a wavelength-dependent photodetector. (a) The response to a square wave for increasing wavelength at 100000 Hz, with increasing loss of amplitude. (b) Relative loss of amplitude as function of frequency for the different wavelengths. [Reproduced (with modifications) from Paper III with the permission of IOP Publishing]

2.3.2 Phase shifts

Phase shifts describe the mismatch in timing between the reference and the signal supplied by the detector. The phase shift can be of three types. Firstly, a frequency-independent phase shift with a fixed value, θ_0 , can be introduced as the function generator generates a periodic function with the same frequency as the reference. Depending on the triggering method and other settings the waves do not necessarily match in phase. Similarly, a phase shift can occur between the driver unit for the optical modulator and the resulting modulated beam.

Secondly, all electronics in the setup are expected to have a certain reaction time, Δt , between receiving a periodic signal and conveying the signal to the next component of the setup. This time does not depend on the frequency, but the signal will be more strongly affected as Δt becomes closer to the period at higher frequencies. The delay will shift a pure sine wave $\sin(\omega t)$ to $\sin(\omega(t - \Delta t))$, corresponding to a phase shift of $-\omega\Delta t$.

Thirdly, some phase shifts may be of a more complex form, such as those caused by a slow photodetector. Here each photon incident on the detector will experience a different delay time, described by some type of distribution. If the delay times follow an exponential distribution the results will, from Equation 2.13, be a phase shift of $-\arctan(\omega\tau_d)$.

By guiding modulated pump light onto the detector and scanning all modulation frequencies the user can identify any phase shifts occurring. If the detector has a wavelength dependence, correcting for phase shifts requires calibrating with the same optical modulator and the same wavelength as the one at which PA is measured. An illustration of phase shifts is shown in Figure 2.8b, using an example of $\theta_0 + \omega\Delta t + \arctan(\omega\tau_d)$. At low frequencies $\arctan(\omega\tau_d) \rightarrow \omega\tau_d$ and the slope of the curve corresponds to $\Delta t + \tau_d$. If τ_d is known from other measurements, such as the loss of radius, the slope can be used to determine Δt . Extrapolating the linear fit to $\omega = 0$ gives θ_0 . Even if no analytical function is available, one can use a measured phase shift curve to correct the data.

After the phase shift as function of frequency is determined we can correct our data. By calculating the phase of the raw signal given by the lock-in amplifier and subtracting the phase shift we obtain the actual phase and can calculate the actual PA_I and PA_Q . This is illustrated in Figure 2.8a.

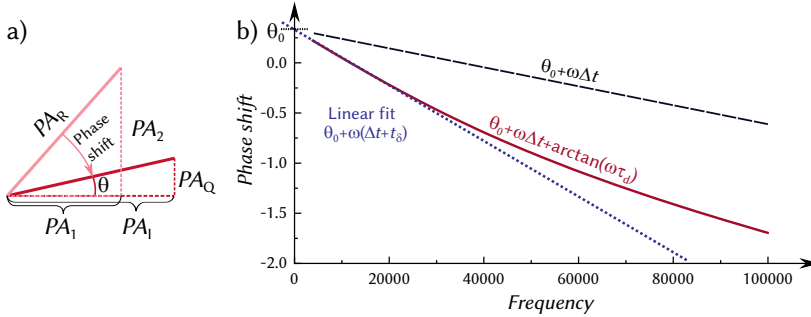


Figure 2.8: (a) Illustration of how the phase shift relates to the raw phases (PA_I and PA_Q) recorded by the lock-in amplifier. To calculate PA_I and PA_Q , defined by the actual phase θ , we must subtract the phase shift. (b) Example of phase shift as function of frequency. The dashed black line shows the phase shift from a constant shift θ_0 and a setup delay Δt . The full red line shows the impact when adding a detector contributing $\arctan(\omega\tau_d)$. At low frequencies this term is linear and, together with Δt , defines the slope.

2.4 RESULTS FROM CWPA

In this section I present a set of measurements where cwPA was used, with a focus on frequency dependence. All measurements were performed on or-

ganic polymer:fullerene blends. The second section showcases the corrections needed for a slow detector at high frequencies.

2.4.1 *Identifying the recombination mechanism from low-frequency quadrature*

The first example (from Paper II) focuses on identifying the recombination mechanism by utilizing the low-frequency quadrature with square-wave modulation. The probe wavelength was chosen as 1025 nm (1.21 eV), after identifying that with polaron absorption P_2 . This transition, alongside the P_1 transition at 0.33 eV, is seen in the spectra in Figure 2.9. Both datasets are from pBTTT:PC₆₀BM[†], prepared as 1:1 and 1:4 blends, respectively.

The frequency dependence, shown in Figure 2.10, displays temperature-dependent behaviour for 1:1 and temperature-independent slopes for 1:4. This was attributed to different dominating recombination mechanisms. The 1:4 case can be explained with a constant $\delta = 2.5$, consistent with 2D Langevin recombination. The temperature-dependent dataset points towards trap-assisted recombination. A close match was found with an exponential distribution with a characteristic energy of $E_{\text{ch}} = 45$ meV. Intensity-dependent measurements, presented in Paper II, corroborated this finding, which also match measurements with other techniques [61]. Any thermal broadening of the trap distribution was not considered in the analysis at the time [26]. This could explain the deviation from simulated slopes, but the dataset is too small for conclusions.

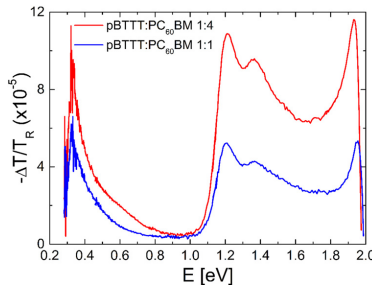


Figure 2.9: The cwPA-spectrum for pBTTT:PC₆₀BM.

[Reproduced from Paper II with the permission of AIP Publishing]

[†] poly[2,5-bis(3-tetradecylthiophen-2-yl)thieno[3,2-b]thiophene]:[6,6]-phenyl-C61-butyric acid methyl ester

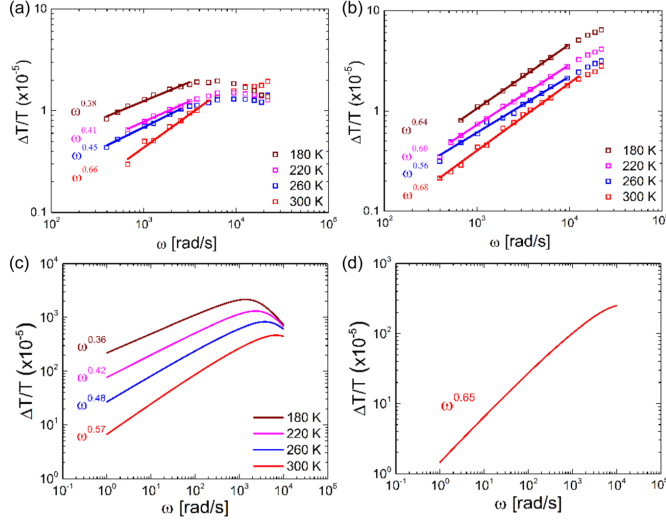


Figure 2.10: Low-frequency PA_Q for square-wave modulation for pBTTT:PC₆₀BM. Measured (a) 1:1 blend, (b) 1:4 blend and simulations with (c) trap-assisted recombination with an exponential distribution ($E_{\text{ch}} = 45$ meV), and (d) 2D Langevin recombination ($\delta = 2.5$). [Reproduced from Paper II with the permission of AIP Publishing]

2.4.2 Determining generation and lifetime from frequency dependence

In the second example (papers III and IV) temperature-dependent generation using sinusoidal modulation is measured over a wide frequency range. These measurements were made on P3HT:ICBA[‡] at different temperatures. Here we employed the corrections for a slow detector discussed above. The detector had a wavelength dependence, illustrated in Figure 2.7. We studied polaron absorption at 985 nm (a P_2 transition) corrected with a detector response evaluated at 980 nm. The corrections impact the data significantly, as shown in Figure 2.11. The raw data showed a high-frequency slope for PA_R (which approach PA_Q at $\omega\tau \gg 1$) of $\omega^{-1.07}$. Any value below -1 is unphysical and can not be recreated by any of the equations presented earlier. After correcting for the losses caused by detector slowness we recover a slope of -0.81 , consistent with Equation 2.12 with $\alpha = 0.81$.

The value of PA_R at high frequencies (which approaches PA_Q at $\omega\tau \gg 1$) is directly proportional to the generation (but independent of lifetime). In

[‡] poly(3-hexylthiophene):indene-C60 bisadduct

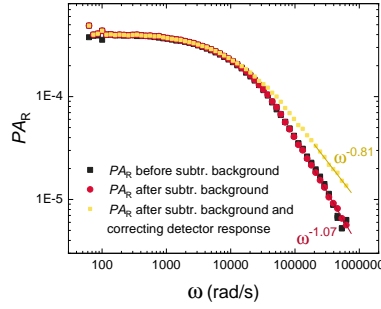


Figure 2.11: Example of how corrections impact the radius signal (P3HT:ICBA). Plot shows raw data (black), data after subtracting frequency-dependent background signals (red) and data after correcting for detector slowness (yellow). [Reproduced from Paper III with the permission of IOP Publishing]

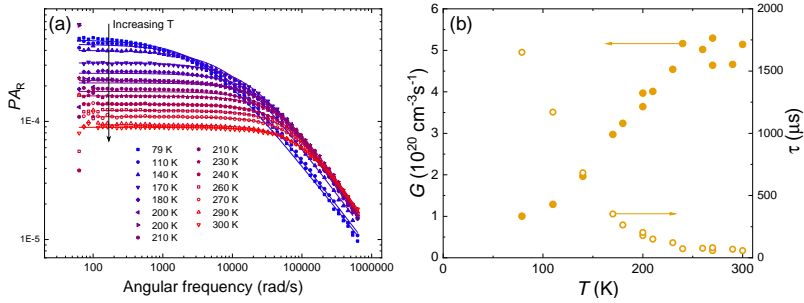


Figure 2.12: (a) Temperature-dependent PA_R for P3HT:ICBA with fits using equations 2.11–2.12. (b) Resulting generation rate and lifetime. [Reproduced (with modifications) from Paper IV with the permission of IOP Publishing]

Figure 2.12a this value is seen to increase and then saturate with increasing temperature, giving immediate insight into the dynamics. The low-frequency saturation value (where $PA_R \rightarrow PA_I$), which depends linearly on the product of generation and lifetime, decreases with increasing temperature, indicating that the lifetime decreases faster than the generation increases with rising temperature. Fitting the curves with PA_R from equations 2.11–2.12 gives the generation and lifetime presented in Figure 2.12b (α presented in supplemental material of Paper IV). As expected from the qualitative analysis, the generation rises with increasing temperature and saturates around 220 K, while the lifetime has a strong dependence on temperature, typical of trap-assisted recombination.

The third example (papers III and IV), from PTB7:PCBM[†], also investigates temperature-dependent generation with sinusoidal modulation but was analysed slightly differently. Contrary to the P3HT:ICBA sample, the detector used here was found to follow the behaviour of Equation 2.13 with a constant τ_d across several wavelengths. This meant that we could make the necessary phase corrections and recover PA_I and PA_Q as separate signals. Figure 2.13a shows that the uncorrected slope of PA_R was -1.38 , decisively below the -1 limit, but after corrections a slope of -0.78 was recovered. Compared to P3HT:ICBA, the “knee” connecting the low and high-frequency regimes was much broader and fell at a higher frequency, as shown in Figure 2.13b. Thus, we were not reaching $\omega\tau \gg 1$ and can not make immediate conclusions about the generation.

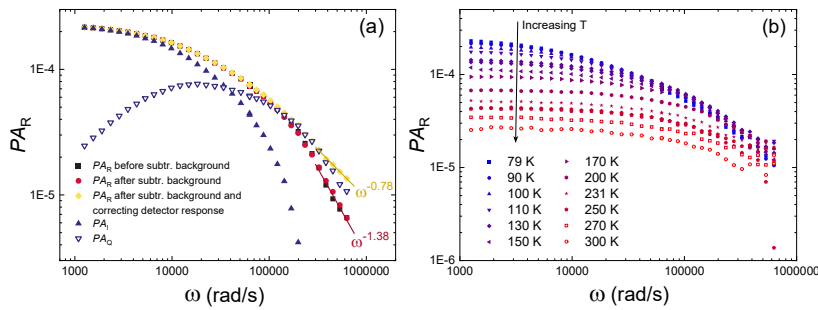


Figure 2.13: (a) PA_R for PTB7:PCBM before and after correcting for background signals and detector slowness, alongside resulting PA_I and PA_Q . (b) Temperature-dependent PA_R . [Reproduced (with modifications) from Papers III and IV with the permission of IOP Publishing]

The broadness of the knee suggested the presence of several absorbing species, with different τ . Therefore, the fits, shown in Figure 2.14a, were implemented by using a sum of two sets of equations 2.9–2.10. Dispersion was excluded to avoid overfitting. The resulting generation rates and lifetimes are shown in Figure 2.14b. The procedure and results are similar to those of Koerner et al. in quaterthiophene: C_{60} films, where a $G(t)$ with a maximum around 150 K was attributed to triplets [62].

[†] Poly[[4,8-bis[(2-ethylhexyl)oxy]benzo[1,2-b:4,5-b']dithiophene-2,6-diyl][3-fluoro-2-[(2-ethylhexyl)carbonyl]thieno[3,4-b]thiophenediyl]]:[6,6]-phenyl-C₆₁-butyric acid methyl ester

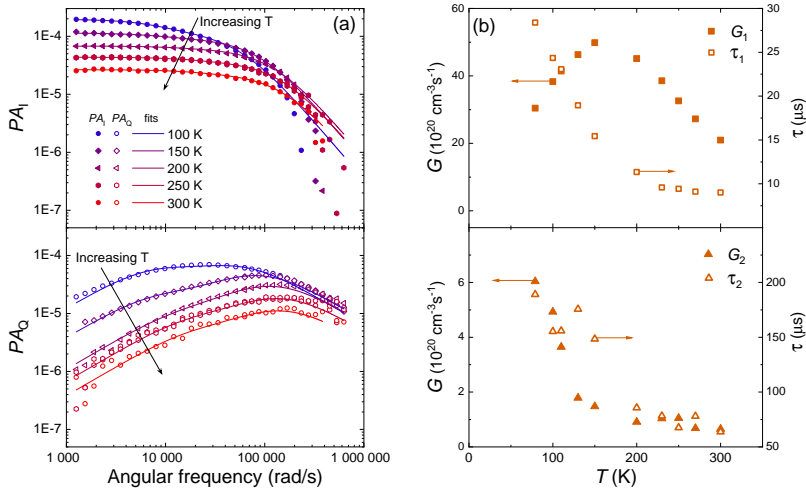


Figure 2.14: (a) Temperature-dependent PA_I and PA_Q for PTB7:PCBM fitted with two sets of equations 2.9–2.10 (only a selection of temperatures shown for clarity). (b) Resulting generation rates and lifetimes for the two species. [Reproduced (with modifications) from Paper IV with the permission of IOP Publishing]

ELECTROMODULATED-PHOTOLUMINESCENCE QUANTUM EFFICIENCY

ELECTROMODULATED-PHOTOLUMINESCENCE quantum efficiency (EM-PLQY) is a measurement method for determining the quasi Fermi level splitting of a solar cell under operational conditions. It is conducted under illumination at V_{OC} , and thus near to the conditions at which the solar cell would be used. The method is based on keeping an illuminated sample at V_{OC} and inducing a small sinusoidal current, as illustrated in Figure 3.1. The current will cause a small periodic luminescence signal which can be detected with the help of a lock-in amplifier. As we know the injected current and the flux of photons coming out of the sample we, can calculate the quantum efficiency.

The luminescence caused by free charge carriers in a solar cell depends on their density, described by the QFLS. Therefore, we can access the QFLS by observing emitted photons. Looking at luminescence from a small number of injected carriers ensures that we observe a signal from free carrier recombination, rather than from excitons. By comparing V_{QFLS} to V_{OC} we can detangle properties of the photovoltaic material from those of the contacts.

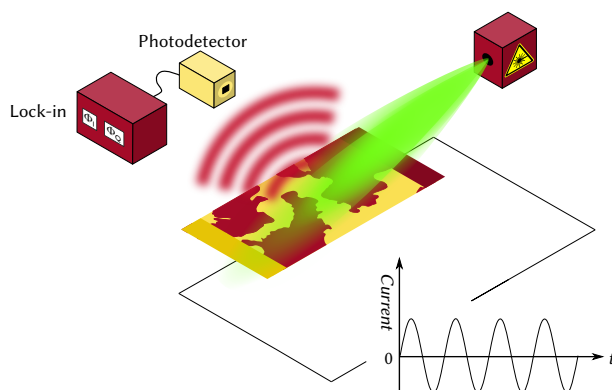


Figure 3.1: Schematic of the EM-PLQY-setup. A sinusoidal current through an illuminated solar cell leads to sinusoidal photoluminescence, detected by a photodetector and lock-in amplifier.

3.1 THEORY OF EM-PLQY

The following derivation is based on the work of Rau [63]. As discussed in Section 1.2, the quasi Fermi level splitting defines the maximum achievable open-circuit voltage. At the radiative limit, where there is no non-radiative losses at the contacts or in the bulk, the QFLS coincides with $V_{\text{OC}}^{\text{rad}}$. Any non-radiative recombination intrinsic to the active layer will decrease the carrier density and lower the quasi Fermi level splitting as

$$qV_{\text{QFLS}} = qV_{\text{OC}}^{\text{rad}} - q\Delta V_{\text{OC}}^{\text{NR,intr}}, \quad (3.1)$$

where $\Delta V_{\text{OC}}^{\text{NR,intr}}$ is the voltage loss due to non-radiative recombination in the bulk. In EM-PLQY the device is kept under illumination, described by the ideal diode Equation 1.7

$$J = J_0 \left(e^{qV/kT} - 1 \right) - J_{\text{L}},$$

where J_0 is the dark saturation current density, V is the voltage over the device, and J_{L} is the photoinduced current density. When $e^{qV/kT} \gg 1$ the second term in the parenthesis can be omitted. Solving for V gives

$$V = \frac{kT}{q} \ln \frac{J + J_{\text{L}}}{J_0}. \quad (3.2)$$

At open-circuit conditions in a solar cell with only radiative recombination, $V = V_{\text{OC}}^{\text{rad}}$ and the current density J is zero.

$$V_{\text{OC}}^{\text{rad}} = \frac{kT}{q} \ln \frac{J_{\text{L}}}{J_{\text{rad},0}}, \quad (3.3)$$

where $J_{\text{rad},0}$ is the dark saturation current density in a device with only radiative recombination.

The quantum efficiency of an LED is defined as the flux of photons emitted, i.e. radiative recombination current density, per electrons injected $\eta_{\text{LED}} = J_{\text{rad}}/J_{\text{inj}}$. As J_{rad} is proportional to the injected current it can be rewritten via Equation 1.7 (with $J_{\text{L}} = 0$ and $e^{qV/kT} \gg 1$),

$$\ln \eta_{\text{LED}} = \ln \frac{J_{\text{rad}}}{J_{\text{inj}}} \approx \ln \frac{J_{\text{rad},0} \exp(qV/kT)}{J_{\text{inj}}} = \frac{qV}{kT} + \ln \frac{J_{\text{rad},0}}{J_{\text{inj}}}. \quad (3.4)$$

Assume that the device is put under illumination, leading to a photogenerated current, and the voltage is adjusted until no current flows through it. At these open-circuit conditions, the injected current equals the photogenerated current.

$$\ln \eta_{\text{LED}} = \frac{qV_{\text{OC}}}{kT} + \ln \frac{J_{\text{rad},0}}{J_{\text{L}}} = \frac{q}{kT} \left(V_{\text{OC}} - V_{\text{OC}}^{\text{rad}} \right), \quad (3.5)$$

where the second term has been rewritten using Equation 3.3. The loss of open-circuit voltage due to non-radiative losses is

$$\Delta V_{\text{OC}}^{\text{NR}} = V_{\text{OC}}^{\text{rad}} - V_{\text{OC}} = -\frac{kT}{q} \ln \eta_{\text{LED}}. \quad (3.6)$$

Assume that instead of operating the device as an LED, we operate it under EM-PLQY conditions. We define a new quantum efficiency η_{EMPL} , as the number of photons emitted per electrons injected as a small perturbation current. As the current is very small the device essentially remains at V_{OC} , and all recombination happens in the bulk, i.e. $\Delta V_{\text{OC}}^{\text{NR}} \rightarrow \Delta V_{\text{OC}}^{\text{NR}, \text{intr}}$. The validity of these substitutions is verified by simulations in Paper V. Substituting the terms in Equation 3.6 and inserting into Equation 3.1 gives

$$qV_{\text{QFLS}} = qV_{\text{OC}}^{\text{rad}} + kT \ln \eta_{\text{EMPL}}, \quad (3.7)$$

relating the EM-PLQY-measurement to the quasi Fermi level splitting. To acquire V_{QFLS} we also need $V_{\text{OC}}^{\text{rad}}$. This can be calculated by finding out the photovoltaic external quantum efficiency of the device and integrating over the black body and sun spectra, as described in the supplemental material of Paper V. A discussion of how EM-PLQY differs from determining QFLS from photoluminescence quantum yield in inorganic materials has been presented by Riley [64].

3.2 MEASURING EM-PLQY

The EM-PLQY-setup is schematically illustrated in Figure 3.1. During the measurement, a small sinusoidal voltage is applied to the sample around the open-circuit voltage. This results in a current density that oscillates around 0 with a small amplitude ΔJ . The solar cell will emit a photoluminescence Φ_{PL} with a small periodic component

$$J_{\text{sample}}(t) = \Delta J \sin(\omega t) \quad (3.8)$$

$$\Phi_{\text{PL}}(t) = \Phi_{\text{PL},0} + \Delta \Phi_{\text{PL}} \sin(\omega t). \quad (3.9)$$

The voltage perturbation is kept so small that $\Delta J < 0.1J_{SC}$. If the injected current is too large the physics no longer correspond to open-circuit conditions. That 10 % is small enough is verified in the supplemental material of Paper V. The collected luminescence is used to calculate the quantum efficiency as

$$\eta_{EMPL} = \frac{q\Delta\Phi_{PL}}{\Delta J}. \quad (3.10)$$

To set up EM-PLQY the values of V_{OC} and J_{SC} need to be known. As the goal is to be close to operating conditions under 1 sun, these values are first measured under a solar simulator. Using this for calibration, we adjust the pump laser intensity so that I_{SC} under the laser equals that under 1 sun.

Similar to cwPA, this measurement employs a lock-in amplifier to gain high sensitivity from a periodic signal. A function generator is used to create a sinusoidally varying voltage over the sample. Between the function generator and the sample, there is an oscilloscope monitoring the conditions. By adjusting the amplitude and offset of the sine wave, the current and voltage are kept at the desired values. The sample is kept under constant illumination by a laser, to ensure it is close to operational conditions. The photoluminescence is collected by a silicon detector, shielded by a long-pass filter to keep scattered laser light from entering. The signal is pre-amplified and passed to the lock-in amplifier, which selects the part of the signal with the frequency ω . In contrast to cwPA, here we only analyse the radius signal and not the phases separately.

In order to obtain an absolute value for η_{EMPL} we need to know what fraction of the photoluminescence we are collecting. A large portion of the photoluminescence will not hit the detector due to the geometry of the setup, and the signal amplitude for different wavelengths is not uniform. To investigate the losses, we measure the quantum efficiency of electroluminescence in the same setup, as discussed in Paper V. This is then repeated inside an integrating sphere (Paper V, SIII). The ratio between the quantum efficiencies gives us the fraction of light that we pick up in the EM-PLQY-measurement. After the correction, η_{EMPL} is calculated via Equation 3.10.

3.3 EXPERIMENTAL VERIFICATION

To verify that the setup allows access to the QFLS, it was applied to several samples. They all had the same photovoltaic material, PM6:Y6[†], but different cathodes. The contact materials have different work functions, and therefore injection barriers ϕ_{cat} . The materials with higher barriers exhibit lower V_{OC} . The QFLS, on the other hand, is not affected by the contacts. The results, discussed in detail in Paper V, are shown in Figure 3.2. The materials show different V_{OC} , but QFLS, extracted from EM-PLQY, stays constant throughout. Paper V also presents drift-diffusion simulations of EM-PLQY, which show excellent agreement between measured and simulated QFLS.

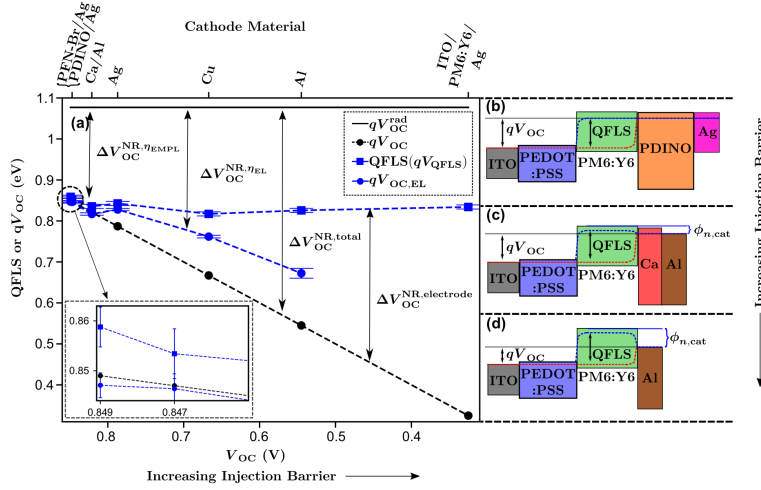


Figure 3.2: Comparison between QFLS from the EM-PLQY-measurement (blue squares) and V_{OC} (black circles and lower x-axis) for contacts with different injection barriers. The different cathode materials are listed on the upper x-axis, with three examples illustrated as energy levels in (b–d). [Reproduced from Paper V under CC BY 4.0 licence]

[†] poly[(2,6-(4,8-bis(5-(2-ethylhexyl-3-fluoro)thiophen-2-yl)-benzo[1,2-b:4,5-b']dithiophene))-alt-(5,5-(1',3'-di-2-thienyl-5',7'-bis(2-ethylhexyl)benzo[1',2'-c:4',5'-c']dithiophene-4,8-dione):2,2'-((2Z,2'Z)-((12,13-bis(2-ethylhexyl)-3,9-diundecyl-12,13-dihydro-[1,2,5]thiadiazolo[3,4-e]thieno[2',3':g]thieno[2',3':4,5]thieno[3,2-b]indole-2,10-diyl)bis(methanylylidene))bis(5,6-difluoro-3-oxo-2,3-dihydro-1H-indene-2,1-diylidene))dimalononitrile

SUMMARY

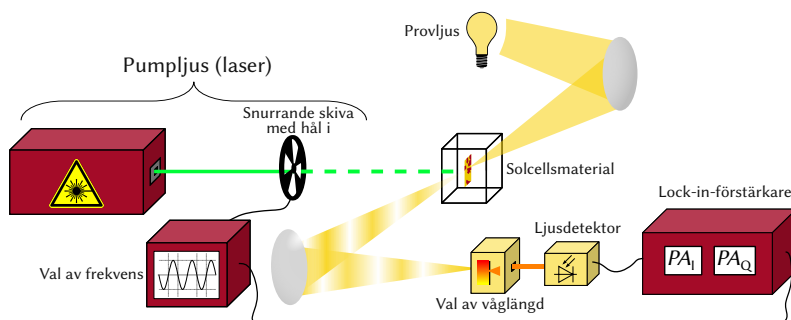
This work has presented new ways of using modulation spectroscopies and applied these to study samples. The main focus has been on continuous-wave photoinduced absorption (cwPA). As a contact-free method, cwPA can help researchers in identifying and characterizing good candidates for solar cells without having to construct complete devices. Using an arbitrary reaction order δ , I have generalized the methods for characterizing recombination in cwPA-data. This yielded the $\omega^{1/(\delta-1)}$ dependence on modulation frequency ω for the quadrature at low frequencies with square-wave modulation. This expression was used to distinguish between trap-assisted and two-dimensional Langevin recombination in films of PBT₃TT:PC₆₀BM with different blend ratios. I also showed that for trap-assisted recombination with an exponential trap distribution the expression depends on the characteristic energy E_{ch} as $\omega^{kT/E_{\text{ch}}}$.

Using a wide span of frequencies and sinusoidal modulation, I extracted generation rates and charge carrier lifetimes from cwPA for a range of temperatures. This revealed distinctly different temperature-dependent generation curves for P3HT:ICBA and PTB7:PCBM. I have described and motivated the procedures necessary to achieve reliable results at high frequencies, especially for slow photodetectors.

Furthermore, I have presented a new type of modulation spectroscopy, electromodulated-photoluminescence quantum efficiency, which can be used to gain access to the quasi Fermi level splitting at open circuit conditions. Combining one photovoltaic material with a range of different contact materials, we showed that the method measures the same QFLS over all devices, despite variations in the open-circuit voltage. The new method offers a way to characterize different losses occurring in solar cells, aiding researchers in optimizing device design.

SAMMANFATTNING PÅ SVENSKA

Den här avhandlingen behandlar mätmetoder som används för att studera solceller. Specifikt handlar den om metoder där provet utsätts för en periodisk påverkan. Av de fem inkluderade artiklarna använder sig fyra av fotoinducerad absorption med kontinuerlig våg (cwPA). Figuren nedan visar en skiss på uppställningen. Detta är en mätmetod där provet undersöks genom att lysa på det med periodiskt varierande ljusstyrka (pumpljus). Man kan säga att vi lyser på solcellsmaterialet med en blinkande laser. Detta ljus lösgör elektroner så att de kan röra sig fritt inne i materialet. Samtidigt lyser man genom provet med annan lampa, med lägre energi (provljus). De frigjorda elektronerna kommer att absorbera en del av provljuset. Ju mera fria elektroner det finns i materialet, desto större andel av ljuset kommer att absorberas. Det här ger oss möjlighet att få information om fysiken som pågår inne i provet genom att mäta absorptionen. Mängden fria elektroner kommer att variera periodiskt, vilket också ger en periodisk absorption.



Skiss av den experimentella uppställningen för fotoinducerad absorption med kontinuerlig våg. Pumpljuset är en laserstråle som upphackas så att den varierar periodiskt. Provljuset lyses genom provet, där pumpljuset frigjort elektroner, och absorberas delvis av dessa elektroner. Absorptionen analyseras för att berätta hur elektronerna beter sig inne i provet.

Anledningen till att man använder en periodisk ljuskälla är att signalen då kan processeras av en så kallad lock-in-förstärkare. Användaren berättar åt lock-in-förstärkaren med vilken frekvens lasern blinkar och apparaten väljer ut den del av signalen som upprepar sig med samma frekvens. Sedan rap-

porterar den detta i form av två komponenter, i-fas-signal PA_I och kvadratur PA_Q . I-fas-signalen representerar den del av signalen som går i samma takt som pumpljuset, medan kvadraturen visar hur stor del som sackar efter. Det fina med lock-in-förstärkaren är att den gör sig av med alla störningar som inte råkar ha precis den frekvens vi tittar på, vilket ger hög noggrannhet.

För att bättre förstå egenskaper hos de fria laddningarna kan vi ändra frekvensen med vilken pumpljuset blinkar eller dess ljusstyrka. I avhandlingen utnyttjar jag detta för att erhålla nya sätt att bestämma rekombinationsordningen δ . Det här är ett värde som beskriver hur elektroner rekombinerar, d.v.s. återgår från det fria tillståndet till att vara bundna. Man kan också undersöka hur länge en elektron typiskt hålls i sitt fria tillstånd eller hur mycket elektroner som frigörs per sekund.

Avhandlingen introducerar också en ny mätmetod, där en liten periodisk växelström leds genom en solcell. Vi undersöker sedan hur provets fotoluminescens reagerar på denna ström för att bättre förstå materialets egenskaper. Även här utnyttjar vi en lock-in-förstärkare för att urskilja väldigt små signaler.

BIBLIOGRAPHY

- [1] S. Sze and M.-K. Lee, *Semiconductor devices, physics and technology* (John Wiley & Sons Singapore Pte. Ltd, 2013).
- [2] P. Würfel and U. Würfel, *Physics of solar cells: from basic principles to advanced concepts* (Wiley, 2016).
- [3] J. Nelson, *The physics of solar cells* (Imperial College Press, distributed by World Scientific Publishing Co., 2003).
- [4] P. Caprioglio, M. Stolterfoht, C. M. Wolff, T. Unold, B. Rech, S. Albrecht, and D. Neher, “On the relation between the open-circuit voltage and quasi-Fermi level splitting in efficient perovskite solar cells,” *Advanced Energy Materials* **9**, 1901631 (2019).
- [5] O. J. Sandberg, M. Nyman, and R. Österbacka, “Effect of contacts in organic bulk heterojunction solar cells,” *Phys. Rev. Appl.* **1**, 024003 (2014).
- [6] H. Ma, H.-L. Yip, F. Huang, and A. K.-Y. Jen, “Interface engineering for organic electronics,” *Advanced Functional Materials* **20**, 1371–1388 (2010).
- [7] W. Tress, *Organic solar cells: theory, experiment, and device simulation*, Springer Series in Materials Science (Springer International Publishing, 2014).
- [8] T. Kirchartz and U. Rau, “Detailed balance and reciprocity in solar cells,” *Physica Status Solidi (a)* **205**, 2737–2751 (2008).
- [9] W. Shockley and H. J. Queisser, “Detailed balance limit of efficiency of p-n junction solar cells,” *Journal of Applied Physics* **32**, 510–519 (1961).
- [10] J. Benduhn et al., “Intrinsic non-radiative voltage losses in fullerene-based organic solar cells,” *Nature Energy* **2**, 17053 (2017).
- [11] Q. Liu and K. Vandewal, “Understanding and suppressing non-radiative recombination losses in non-fullerene organic solar cells,” *Advanced Materials* **35**, 2302452 (2023).

- [12] D. Luo, R. Su, W. Zhang, Q. Gong, and R. Zhu, “Minimizing non-radiative recombination losses in perovskite solar cells,” *Nature Reviews Materials* **5**, 44–60 (2020).
- [13] M. Pope and C. Swenberg, *Electronic processes in organic crystals and polymers* (Oxford University Press, New York, 1999).
- [14] M. P. Langevin, “Recombinaison et mobilités des ions dans les gaz,” *Annales de chimie et de physique* **28**, 433–530 (1903).
- [15] G. Juška, K. Genevičius, N. Nekrašas, G. Sliauzys, and R. Österbacka, “Two dimensional Langevin recombination in regioregular poly(3-hexylthiophene),” *Applied Physics Letters* **95**, 013303 (2009).
- [16] M. Westerling, R. Österbacka, and H. Stubb, “Recombination of long-lived photoexcitations in regioregular polyalkylthiophenes,” *Phys. Rev. B* **66**, 165220 (2002).
- [17] T. Kirchartz and J. Nelson, “Meaning of reaction orders in polymer:fullerene solar cells,” *Phys. Rev. B* **86**, 165201 (2012).
- [18] W. Shockley and W. T. Read, “Statistics of the recombinations of holes and electrons,” *Phys. Rev.* **87**, 835–842 (1952).
- [19] R. N. Hall, “Electron-hole recombination in germanium,” *Phys. Rev.* **87**, 387–387 (1952).
- [20] J. A. Willemen, “Modelling of amorphous silicon single- and multi-junction solar cells,” PhD thesis (Delft University of Technology, 1998).
- [21] D. Luo, W. Jang, D. D. Babu, M. S. Kim, D. H. Wang, and A. K. K. Kyaw, “Recent progress in organic solar cells based on non-fullerene acceptors: materials to devices,” *J. Mater. Chem. A* **10**, 3255–3295 (2022).
- [22] A. Armin et al., “A history and perspective of non-fullerene electron acceptors for organic solar cells,” *Advanced Energy Materials* **11**, 2003570 (2021).
- [23] L. J. A. Koster, E. C. P. Smits, V. D. Mihailetschi, and P. W. M. Blom, “Device model for the operation of polymer/fullerene bulk heterojunction solar cells,” *Phys. Rev. B* **72**, 085205 (2005).
- [24] J. Nelson, “Diffusion-limited recombination in polymer-fullerene blends and its influence on photocurrent collection,” *Phys. Rev. B* **67**, 155209 (2003).
- [25] R. C. I. MacKenzie, T. Kirchartz, G. F. A. Dibb, and J. Nelson, “Modeling nongeminate recombination in P3HT:PCBM solar cells,” *The Journal of Physical Chemistry C* **115**, 9806–9813 (2011).

- [26] C. Kaiser, O. J. Sandberg, N. Zarrabi, W. Li, P. Meredith, and A. Armin, “A universal Urbach rule for disordered organic semiconductors,” *Nature Communications* **12**, 3988 (2021).
- [27] A. Miller and E. Abrahams, “Impurity conduction at low concentrations,” *Phys. Rev.* **120**, 745–755 (1960).
- [28] V. Ambegaokar, B. I. Halperin, and J. S. Langer, “Hopping conductivity in disordered systems,” *Phys. Rev. B* **4**, 2612–2620 (1971).
- [29] A. Köhler and H. Bässler, “Triplet states in organic semiconductors,” *Materials Science and Engineering: R: Reports* **66**, 71–109 (2009).
- [30] S. Sandén, N. M. Wilson, E. Wang, and R. Österbacka, “Generation of photoexcitations and trap-assisted recombination in TQ1:PC₇₁BM blends,” *The Journal of Physical Chemistry C* **121**, 8211–8219 (2017).
- [31] A. J. Heeger, S. Kivelson, J. R. Schrieffer, and W. P. Su, “Solitons in conducting polymers,” *Rev. Mod. Phys.* **60**, 781–850 (1988).
- [32] K. Fesser, A. R. Bishop, and D. K. Campbell, “Optical absorption from polarons in a model of polyacetylene,” *Phys. Rev. B* **27**, 4804–4825 (1983).
- [33] R. Österbacka, C. P. An, X. M. Jiang, and Z. V. Vardeny, “Two-dimensional electronic excitations in self-assembled conjugated polymer nanocrystals,” *Science* **287**, 839–842 (2000).
- [34] H. Aarnio, M. Westerling, R. Österbacka, M. Svensson, M. Andersson, and H. Stubb, “Photoinduced absorption in an alternating polyfluorene copolymer for photovoltaic applications,” *Chemical Physics* **321**, 127–132 (2006).
- [35] K. Vandewal, “Interfacial charge transfer states in condensed phase systems,” *Annual Review of Physical Chemistry* **67**, 113–133 (2016).
- [36] M. Cardona, “Modulation spectroscopy of semiconductors,” in *Festkörperprobleme x*, edited by O. Madelung (Springer Berlin Heidelberg, 1970), pp. 125–173.
- [37] F. H. Pollak and H. Shen, “Modulation spectroscopy of semiconductors: bulk/thin film, microstructures, surfaces/interfaces and devices,” *Materials Science and Engineering: R: Reports* **10**, xv–374 (1993).
- [38] Zurich Instruments, *Principles of lock-in detection and the state of the art* (Zurich, Switzerland, 2023).
- [39] Stanford Research Systems, *Model SR830 DSP lock-in amplifier* (Sunnyvale, California, 2011).

- [40] R. K. Willardson and A. C. Beer, *Semiconductors and semimetals* (Academic Press, 1972).
- [41] P. O'Connor and J. Tauc, "Photoinduced midgap absorption in tetrahedrally bonded amorphous semiconductors," *Phys. Rev. B* **25**, 2748–2766 (1982).
- [42] M. Westerling, "Recombination dynamics of long-lived photoexcitations in π -conjugated polymers," PhD thesis (Åbo Akademi University, 2004).
- [43] Z. V. Vardeny and X. Wei, "Optical probes of photoexcitations in conducting polymers," in *Handbook of conducting polymers*, edited by T. A. Skotheim and J. Reynolds (Marcel Dekker, New York, 1997) Chap. 22.
- [44] C. Brabec and V. Dyakonov, "Photoinduced charge transfer in bulk heterojunction," in *Organic photovoltaics, concepts and realization*, edited by C. Brabec, V. Dyakonov, J. Parisi, and N. Sariciftci (Springer Berlin Heidelberg, 2003).
- [45] G. Dellepiane, C. Cuniberti, D. Comoretto, G. F. Musso, G. Figari, A. Piaggi, and A. Borghesi, "Long-lived photoexcited states in symmetrical polydicarbazolyldiacetylene," *Phys. Rev. B* **48**, 7850–7856 (1993).
- [46] C. Botta, S. Luzzati, R. Tubino, D. D. C. Bradley, and R. H. Friend, "Photoinduced absorption of polymer solutions," *Phys. Rev. B* **48**, 14809–14817 (1993).
- [47] M. Westerling, C. Vijila, R. Österbacka, and H. Stubb, "Dispersive and nondispersive recombination of photoexcitations in disordered organic solids," *Phys. Rev. B* **69**, 245201 (2004).
- [48] S. M. Ryvkin, *Photoelectric effects in semiconductors* (Consultants Bureau, New York, 1964).
- [49] I. S. Gradshteyn and I. M. Ryzhnik, *Table of integrals, series and products 6th edition* (Academic Press, San Diego, USA, 2000).
- [50] M. Westerling, C. Vijila, R. Österbacka, and H. Stubb, "Bimolecular recombination in regiorandom poly(3-hexylthiophene)," *Chemical Physics* **286**, 315–320 (2003).
- [51] O. Epshtein, G. Nakhmanovich, Y. Eichen, and E. Ehrenfreund, "Dispersive dynamics of photoexcitations in conjugated polymers measured by photomodulation spectroscopy," *Phys. Rev. B* **63**, 125206 (2001).

- [52] O. Epshtein, Y. Eichen, E. Ehrenfreund, M. Wohlgenannt, and Z. V. Vardeny, "Linear and nonlinear photoexcitation dynamics in π -conjugated polymers," *Phys. Rev. Lett.* **90**, 046804 (2003).
- [53] K. S. Cole and R. H. Cole, "Dispersion and Absorption in Dielectrics I. Alternating Current Characteristics," *The Journal of Chemical Physics* **9**, 98–105 (1941).
- [54] H. Aarnio, M. Westerling, R. Österbacka, M. Svensson, M. R. Andersson, T. Pascher, J. Pan, V. Sundström, and H. Stubb, "Recombination studies in a polyfluorene copolymer for photovoltaic applications," *Synthetic Metals* **155**, 299–302 (2005).
- [55] M. D. Heinemann, K. von Maydell, F. Zutz, J. Kolny-Olesiak, H. Borchert, I. Riedel, and J. Parisi, "Photo-induced charge transfer and relaxation of persistent charge carriers in polymer/nanocrystal composites for applications in hybrid solar cells," *Advanced Functional Materials* **19**, 3788–3795 (2009).
- [56] R. Wang, X. Yang, W. Hong, Y. Wang, H. Li, L. Li, and C.-X. Sheng, "Excited-states spectroscopies and its magnetic field effect of π -conjugated polymer-fullerene blends with below-gap excitation," *Synthetic Metals* **223**, 132–136 (2017).
- [57] J. Cabanillas-Gonzalez, C. Sciascia, G. Lanzani, S. Toffanin, R. Capelli, M. C. Ramon, M. Muccini, J. Gierschner, T.-Y. Hwu, and K.-T. Wong, "Molecular packing effects on the optical spectra and triplet dynamics in oligofluorene films," *The Journal of Physical Chemistry B* **112**, PMID: 18712907, 11605–11609 (2008).
- [58] E. Gershman, T. Drori, C. Herzog, Y. Eichen, and E. Ehrenfreund, "Recombination kinetics of photoexcitations in films of MEH-PPV and MEH-PPV/C60 mixtures," *Synthetic Metals* **154**, 237–240 (2005).
- [59] R. Metzler and J. Klafter, "From stretched exponential to inverse power-law: fractional dynamics, Cole-Cole relaxation processes, and beyond," *Journal of Non-Crystalline Solids* **305**, 81–87 (2002).
- [60] Hamamatsu, *Technical note: Si photodiodes*, Solid state division, Hamamatsu Photonics K.K (Hamamatsu City, Japan, 2022).
- [61] M. Nyman, O. J. Sandberg, and R. Österbacka, "2D and trap-assisted 2D Langevin recombination in polymer:fullerene blends," *Advanced Energy Materials* **5**, 1400890 (2015).

- [62] C. Koerner, H. Ziehlke, R. Gresser, R. Fitzner, E. Reinold, P. Bäuerle, K. Leo, and M. Riede, “Temperature activation of the photoinduced charge carrier generation efficiency in quaterthiophene: C_{60} mixed films,” *The Journal of Physical Chemistry C* **116**, 25097–25105 (2012).
- [63] U. Rau, “Reciprocity relation between photovoltaic quantum efficiency and electroluminescent emission of solar cells,” *Phys. Rev. B* **76**, 085303 (2007).
- [64] D. Riley, “On the relation between exciton dynamics and nano-morphology in organic semiconductor blends,” PhD thesis (Swansea University, 2023).

Nora M. Wilson

Modulation Spectroscopies for Characterization of Photovoltaic Materials and Devices

This thesis presents new ways of characterizing photovoltaic semiconductors and devices using modulation spectroscopies. The main part of the thesis concerns continuous-wave photoinduced absorption (cwPA). This is a contact-free optical pump-probe technique, using a modulated laser for creating photoexcitations in the material. I provide new routes to information about recombination, through determining the reaction order, and a toolbox for obtaining reliable cwPA-data despite imperfect equipment. In addition to cwPA, a new method, called electromodulated-photoluminescence quantum efficiency, is presented. In this, a solar cell is subjected to a small periodic voltage while the photoluminescence is measured. From the measurement we can determine the quasi Fermi level splitting of a photovoltaic material.

ISBN 978-952-12-4366-0